INTERNATIONAL JOURNAL FOR NUMERICAL METHODS IN FLUIDS
*Int. J. Numer. Meth. Fluids* 2008; **57**:601–629
Published online 25 October 2007 in Wiley InterScience (www.interscience.wiley.com). DOI: 10.1002/fld.1633

# Arterial fluid mechanics modeling with the stabilized space–time fluid–structure interaction technique

Tayfun E. Tezduyar[1,*,†], Sunil Sathe[1], Matthew Schwaab[1] and Brian S. Conklin[1,2]

[1]*Team for Advanced Flow Simulation and Modeling (T★AFSM), Mechanical Engineering, Rice University – MS 321, 6100 Main Street, Houston, TX 77005, U.S.A.*
[2]*Sections of Leukocyte Biology and Nutrition, Department of Pediatrics, Baylor College of Medicine, Children's Nutrition Research Center, 1100 Bates, Suite 6014, Houston, TX 77030, U.S.A.*

SUMMARY

We present an overview of how the arterial fluid mechanics problems can be modeled with the stabilized space–time fluid–structure interaction (SSTFSI) technique developed by the Team for Advanced Flow Simulation and Modeling (T★AFSM). The SSTFSI technique includes the enhancements introduced recently by the T★AFSM to increase the scope, accuracy, robustness and efficiency of this class of techniques. The SSTFSI technique is supplemented with a number of special techniques developed for arterial fluid mechanics modeling. These include a recipe for pre-FSI computations that improve the convergence of the FSI computations, using an estimated zero-pressure arterial geometry, and the sequentially coupled arterial FSI (SCAFSI) technique. The recipe for pre-FSI computations is based on the assumption that the arterial deformation during a cardiac cycle is driven mostly by the blood pressure. The SCAFSI technique, which was introduced as an approximate FSI approach in arterial fluid mechanics, is also based on that assumption. The need for an estimated zero-pressure arterial geometry is based on recognizing that the patient-specific image-based geometries correspond to time-averaged blood pressure values. In our arterial fluid mechanics modeling the arterial walls can be represented with the membrane or continuum elements, both of which are geometrically nonlinear, and the continuum element is made of hyperelastic (Fung) material. Test computations are presented for cerebral and abdominal aortic aneurysms, where the arterial geometries used in the computations are close approximations to the patient-specific image-based data. Copyright © 2007 John Wiley & Sons, Ltd.

Received 16 July 2007; Revised 5 September 2007; Accepted 6 September 2007

KEY WORDS: cardiovascular fluid mechanics; cerebral aneurysms; fluid–structure interactions; hyper elastic material; space–time methods

*Correspondence to: Tayfun E. Tezduyar, Team for Advanced Flow Simulation and Modeling (T★AFSM), Mechanical Engineering, Rice University – MS 321, 6100 Main Street, Houston, TX 77005, U.S.A.
†E-mail: tezduyar@rice.edu

Contract/grant sponsor: John & Ann Doerr Fund for Computational Biomedicine
Contract/grant sponsor: NSF; contract/grant number: CNS-0421109
Contract/grant sponsor: NIH/NHLBI; contract/grant number: HL73868
Contract/grant sponsor: USDA; contract/grant number: 6250-51000-046

## 1. INTRODUCTION

Much has been accomplished in arterial fluid mechanics modeling in recent years (see, for example, [1–10]), and many of the computational challenges involved are being addressed with the advances we see in computational mechanics. One of the major computational challenges is accurate and efficient modeling of the fluid–structure interactions (FSI) between the blood flow and arterial walls. We have been seeing a good number of articles in FSI modeling since the early 1990s (see, for example, [3, 6, 11–43]). For most researchers the preferred method of handling the moving interfaces involved in FSI modeling has been the arbitrary Lagrangian–Eulerian finite element formulation [44].

For the Team for Advanced Flow Simulation and Modeling (T★AFSM),[‡] the preferred method of handling the moving interfaces involved in FSI modeling has been the deforming-spatial-domain/stabilized space–time (DSD/SST) formulation [11–13, 19], which was introduced by the T★AFSM in 1991 as a general-purpose interface-tracking (i.e. moving mesh) technique for computation of flow problems with moving boundaries or interfaces. The formulation is based on the streamline-upwind/Petrov–Galerkin (SUPG) [45, 46] and pressure-stabilizing/Petrov–Galerkin (PSPG) [11, 47] methods. An earlier version of the pressure stabilization, for Stokes flows, was introduced in [48]. The SST formulations were introduced and tested earlier by other researchers in the context of problems with fixed spatial domains (see, for example, [49]).

The DSD/SST formulation and the mesh update methods [50–52] developed by the T★AFSM are the core technologies for the space–time FSI techniques developed by the T★AFSM (see, for example, [14, 15, 17, 22, 25, 29, 30, 36]). These space–time FSI techniques have been used in a number of 3D FSI computations in arterial fluid mechanics (see [1, 2, 4, 5, 7]), starting with a journal article [1] published in 2004 by the Japan Society of Mechanical Engineers. These computations mostly focused on cerebral aneurysms, with the arterial models extracted from computed tomography. The blood was assumed to behave like a Newtonian fluid. The arterial structures (walls) were modeled with a continuum element, which was geometrically nonlinear, made of linearly elastic material. The coupled fluid and structural mechanics and mesh-moving equations were solved with a block-iterative coupling technique (see [29, 30, 53] for comparative descriptions of the block-iterative, quasi-direct and direct coupling techniques). The inflow boundary condition used in the computations is a pulsatile velocity profile, which closely represents the measured flow rate during a heartbeat cycle. A brief, chronological review of the computations reported in [1, 2, 4, 5, 7] was provided in [8].

New, enhanced versions of the DSD/SST and space–time FSI techniques were recently introduced in [53] to increase the scope, accuracy, robustness and efficiency of this class of techniques. Several 3D numerical examples computed with these new SSTFSI techniques were also reported in [53]. The new SSTFSI techniques were extended in [8] to FSI modeling in arterial fluid mechanics. The choices for the structural models used in [53] for the arterial walls were the membrane and continuum elements, both geometrically nonlinear, and the material-model choices for the continuum element were linearly elastic and hyperelastic (Mooney–Rivlin) models.

Our more recent test computations showed that when the arterial wall thickness falls below some level, the computations with the continuum element made of linearly elastic material become

[‡]This team name was intended to imply the research team led by Tezduyar also prior to when the team assumed this specific name.



DOI: 10.1002/fld

unstable when the blood pressure exceeds some level. This observation is consistent with what was pointed out to us recently by Hughes [54]—that this is not a suitable material model when the strains are not infinitesimal, especially if there are compressive strains. Therefore, we are not pursuing the linearly elastic material model further and instead placing even a greater emphasis on the hyperelastic models. The results reported in [8] for the Mooney–Rivlin material, where the two Mooney–Rivlin constants were determined in a spontaneous fashion, showed larger deformations than the other two structural models used in [8]. In [55], for the two Mooney–Rivlin constants, we used values determined in a more systematic way based on the test data reported in [56]. The model used in [56] involves five constants. In [55], we determined the two constants we use based on those five parameters and the strain energy considerations. Although this made the deformations much more comparable with those obtained with the other two structural models used in [8], we were still not fully satisfied with using a Mooney–Rivlin material model in our arterial fluid mechanics computations. That, and what we see in the literature, convinced us to move to a hyperelastic material model of Fung type.

Our recent experiences with the arterial fluid mechanics computations also helped us introduce a number of special techniques targeting specifically arterial fluid mechanics modeling. These include using an estimated zero-pressure arterial geometry [57], a recipe for pre-FSI computations [8] that improve the convergence of the FSI computations and the sequentially coupled arterial FSI (SCAFSI) technique [58]. These special techniques are described in Sections 4–7.

The governing equations and the finite element formulations, including the DSD/SST and SSTFSI techniques, are described in Sections 2 and 3. The fluid (blood) and structure (arterial wall) properties and boundary conditions are given in Section 5. The test computations are reported in Section 8. They are for cerebral and abdominal aortic aneurysms, where the arterial geometries used in the computations are close approximations to the patient-specific image-based data. Our objective in these test computations is not to conduct arterial fluid mechanics studies at a level of detail seen in [1, 2, 4, 5, 7, 10]. Rather, our objective is to test the new SSTFSI techniques and the special techniques targeting specifically arterial fluid mechanics and show that these techniques can successfully deal with different types of arterial problems and structural models. Concluding remarks are given in Section 9.

## 2. GOVERNING EQUATIONS

### 2.1. Fluid mechanics (blood flow)

Although the blood is known to be non-Newtonian in general, we are assuming it to be Newtonian here. The explanation we give for that here has been reproduced from the explanation given in [10]. For the arterial diameters and flow rates we consider in this paper, the average shear rate in the artery is larger than $150\,\mathrm{s}^{-1}$. As it was pointed out in [10], the viscosity of the blood can be assumed to be constant if the shear rate is high enough ($>150\,\mathrm{s}^{-1}$) [59].

Let $\Omega_t \subset \mathbb{R}^{n_{sd}}$ be the spatial domain with boundary $\Gamma_t$ at time $t \in (0, T)$. The subscript $t$ indicates the time dependence of the domain. The Navier–Stokes equations of incompressible flows are expressed on $\Omega_t$ and $\forall t \in (0, T)$ as

$$\rho\left(\frac{\partial \mathbf{u}}{\partial t} + \mathbf{u}\cdot\nabla\mathbf{u} - \mathbf{f}\right) - \nabla\cdot\boldsymbol{\sigma} = \mathbf{0} \tag{1}$$

$$\nabla\cdot\mathbf{u} = 0 \tag{2}$$



DOI: 10.1002/fld

where $\rho$, $\mathbf{u}$ and $\mathbf{f}$ are the density, velocity and external force, respectively. The stress tensor $\boldsymbol{\sigma}$ is defined as $\boldsymbol{\sigma}(p,\mathbf{u})=-p\mathbf{I}+2\mu\boldsymbol{\varepsilon}(\mathbf{u})$, with $\boldsymbol{\varepsilon}(\mathbf{u})=((\nabla\mathbf{u})+(\nabla\mathbf{u})^{\mathrm{T}})/2$. Here $p$ is the pressure, $\mathbf{I}$ is the identity tensor, $\mu=\rho\nu$ is the viscosity $\nu$ is the kinematic viscosity and $\boldsymbol{\varepsilon}(\mathbf{u})$ is the strain-rate tensor. The essential and natural boundary conditions for Equation (1) are represented as $\mathbf{u}=\mathbf{g}$ on $(\Gamma_t)_g$ and $\mathbf{n}\cdot\boldsymbol{\sigma}=\mathbf{h}$ on $(\Gamma_t)_h$, where $(\Gamma_t)_g$ and $(\Gamma_t)_h$ are complementary subsets of the boundary $\Gamma_t$, $\mathbf{n}$ is the unit normal vector, and $\mathbf{g}$ and $\mathbf{h}$ are given functions. A divergence-free velocity field $\mathbf{u}_0(\mathbf{x})$ is specified as the initial condition.

### 2.2. Structural mechanics (arterial wall deformation)

Let $\Omega_t^{\mathrm{s}}\subset\mathbb{R}^{n_{xd}}$ be the spatial domain with boundary $\Gamma_t^{\mathrm{s}}$, where $n_{xd}=3$ for the continuum element and $n_{xd}=2$ for the membrane element. The superscript '$s$' indicates the structure. The parts of $\Gamma_t^{\mathrm{s}}$ corresponding to the essential and natural boundary conditions are represented by $(\Gamma_t^{\mathrm{s}})_g$ and $(\Gamma_t^{\mathrm{s}})_h$. The equations of motion are expressed as

$$\rho^{\mathrm{s}}\left(\frac{\mathrm{d}^2\mathbf{y}}{\mathrm{d}t^2}+\eta\frac{\mathrm{d}\mathbf{y}}{\mathrm{d}t}-\mathbf{f}^{\mathrm{s}}\right)-\nabla\cdot\boldsymbol{\sigma}^{\mathrm{s}}=\mathbf{0} \tag{3}$$

where $\rho^{\mathrm{s}}$, $\mathbf{y}$, $\eta$, $\mathbf{f}^{\mathrm{s}}$ and $\boldsymbol{\sigma}^{\mathrm{s}}$ are the material density, structural displacement, damping coefficient, external force and Cauchy stress tensor, respectively. The stresses are expressed in terms of the second Piola–Kirchoff stress tensor $\mathbf{S}$, which is related to the Cauchy stress tensor through a kinematic transformation. For the arterial structural models we cover here, what makes one structural element model different from the other is the manner in which $\mathbf{S}$ is defined.

*2.2.1. Membrane element.* Under the assumption of large displacements and rotations, small strains and no material damping, the membranes are characterized with linearly elastic material properties. Under the assumption of plane stress, $\mathbf{S}$ becomes

$$S^{ij}=(\bar{\lambda}^{\mathrm{s}}G^{ij}G^{kl}+\mu^{\mathrm{s}}(G^{il}G^{jk}+G^{ik}G^{jl}))E_{kl} \tag{4}$$

where for the case of isotropic plane stress $\bar{\lambda}^{\mathrm{s}}=2\lambda^{\mathrm{s}}\mu^{\mathrm{s}}/(\lambda^{\mathrm{s}}+2\mu^{\mathrm{s}})$, and the strain tensor is defined as

$$E_{kl}=\tfrac{1}{2}(g_{kl}-G_{kl}) \tag{5}$$

Here, $\lambda^{\mathrm{s}}$ and $\mu^{\mathrm{s}}$ are the Lamé constants, $G^{ij}$ are the contravariant metric tensor components in the undeformed configuration, and $g_{kl}$ and $G_{kl}$ are covariant metric tensor components in the deformed and undeformed configurations.

*2.2.2. Continuum element made of Mooney–Rivlin material.* For the continuum element made of Mooney–Rivlin material, the expression for $\mathbf{S}$ is given as

$$S^{ij}=2(C_1+C_2G^{kl}g_{kl})G^{ij}-2C_2G^{ik}g_{kl}G^{lj}+(K_{\mathrm{PEN}}\ln(\sqrt{I_3})-2(C_1+2C_2))g^{ij} \tag{6}$$

where $C_1$ and $C_2$ are the Mooney–Rivlin material constants, and $g^{ij}$ are the contravariant metric tensor components in the deformed configuration. The incompressibility constraint is enforced with the penalty term $K_{\mathrm{PEN}}\ln(\sqrt{I_3})$ (see [60]). Here $I_3$ is the third invariant of the right Cauchy–Green



DOI: 10.1002/fld

deformation tensor, and $K_{\mathrm{PEN}}$ is a penalty parameter determined based on the expression given in [61] for the bulk modulus:

$$K_{\mathrm{PEN}}=\frac{2(C_1+C_2)}{(1-2\nu_{\mathrm{PEN}})} \tag{7}$$

where $\nu_{\mathrm{PEN}}$ (with a value close to 0.50) is the 'penalty' Poisson ratio we use in the expression in place of the actual Poisson ratio.

*2.2.3. Continuum element made of Fung material.* For the continuum element made of Fung material, the expression for $\mathbf{S}$ is given as

$$S^{ij}=2D_1D_2\,\mathrm{e}^{D_2(I_1-3)}G^{ij}+(K_{\mathrm{PEN}}\ln(\sqrt{I_3})-2D_1D_2)g^{ij} \tag{8}$$

where $I_1$ is the first invariant of the right Cauchy–Green deformation tensor, $D_1$ and $D_2$ are the Fung material constants and $K_{\mathrm{PEN}}$ is defined as

$$K_{\mathrm{PEN}}=\frac{2D_1D_2}{(1-2\nu_{\mathrm{PEN}})} \tag{9}$$

## 3. FINITE ELEMENT FORMULATIONS

### *3.1. DSD/SST formulation of fluid mechanics*

In the DSD/SST method [11–13, 19], the finite element formulation is written over a sequence of $N$ space–time slabs $Q_n$, where $Q_n$ is the slice of the space–time domain between the time levels $t_n$ and $t_{n+1}$. At each time step, the integrations are performed over $Q_n$. The space–time finite element interpolation functions are continuous within a space–time slab, but discontinuous from one space–time slab to another. The notations $(\cdot)_n^-$ and $(\cdot)_n^+$ will denote the function values at $t_n$ as approached from below and above. Each $Q_n$ is decomposed into elements $Q_n^e$, where $e=1,2,\ldots,(n_{\mathrm{el}})_n$. The subscript $n$ used with $n_{\mathrm{el}}$ is for the general case where the number of space–time elements may change from one space–time slab to another. The essential and natural boundary conditions are enforced over $(P_n)_g$ and $(P_n)_h$, the complementary subsets of the lateral boundary of the space–time slab. The finite element trial function spaces $(\mathscr{S}^h_{\mathbf{u}})_n$ for velocity and $(\mathscr{S}^h_p)_n$ pressure, and the test function spaces $(\mathscr{V}^h_{\mathbf{u}})_n$ and $(\mathscr{V}^h_p)_n=(\mathscr{S}^h_p)_n$ are defined by using, over $Q_n$, first-order polynomials in space and time.

The DSD/SST formulation (from [19]) is expressed as follows: given $(\mathbf{u}^h)_n^-$, find $\mathbf{u}^h\in(\mathscr{S}^h_{\mathbf{u}})_n$ and $p^h\in(\mathscr{S}^h_p)_n$ such that $\forall\mathbf{w}^h\in(\mathscr{V}^h_{\mathbf{u}})_n$ and $\forall q^h\in(\mathscr{V}^h_p)_n$:

$$\int_{Q_n}\mathbf{w}^h\cdot\rho\left(\frac{\partial\mathbf{u}^h}{\partial t}\mathbf{u}^h\cdot\nabla\mathbf{u}^h-\mathbf{f}^h\right)\mathrm{d}Q+\int_{Q_n}\boldsymbol{\varepsilon}(\mathbf{w}^h):\boldsymbol{\sigma}(p^h,\mathbf{u}^h)\,\mathrm{d}Q$$
$$-\int_{(P_n)_h}\mathbf{w}^h\cdot\mathbf{h}^h\,\mathrm{d}P+\int_{Q_n}q^h\nabla\cdot\mathbf{u}^h\,\mathrm{d}Q+\int_{\Omega_n}(\mathbf{w}^h)_n^+\cdot\rho((\mathbf{u}^h)_n^+-(\mathbf{u}^h)_n^-)\,\mathrm{d}\Omega$$



DOI: 10.1002/fld

$$+\sum_{e=1}^{(n_{\mathrm{el}})_n}\int_{Q_n^e}\frac{1}{\rho}\left[\tau_{\mathrm{SUPG}}\rho\left(\frac{\partial \mathbf{w}^h}{\partial t}+\mathbf{u}^h\cdot\nabla\mathbf{w}^h\right)+\tau_{\mathrm{PSPG}}\nabla q^h\right]\cdot\left[Ł(p^h,\mathbf{u}^h)-\rho\mathbf{f}^h\right]\mathrm{d}Q$$

$$+\sum_{e=1}^{(n_{\mathrm{el}})_n}\int_{Q_n^e}\nu_{\mathrm{LSIC}}\nabla\cdot\mathbf{w}^h\rho\nabla\cdot\mathbf{u}^h\mathrm{d}Q=0 \tag{10}$$

where

$$Ł(q^h,\mathbf{w}^h)=\rho\left(\frac{\partial \mathbf{w}^h}{\partial t}+\mathbf{u}^h\cdot\nabla\mathbf{w}^h\right)-\nabla\cdot\boldsymbol{\sigma}(q^h,\mathbf{w}^h) \tag{11}$$

This formulation is applied to all space–time slabs $Q_0, Q_1, Q_2, \ldots, Q_{N-1}$, starting with $(\mathbf{u}^h)_0^- = \mathbf{u}_0$. Here $\tau_{\mathrm{SUPG}}$, $\tau_{\mathrm{PSPG}}$ and $\nu_{\mathrm{LSIC}}$ are the SUPG, PSPG and LSIC (least-squares on incompressibility constraint) stabilization parameters. There are various ways of defining these stabilization parameters. Here we provide the definitions given in [19]:

$$\tau_{\mathrm{SUPG}}=\left(\frac{1}{\tau_{\mathrm{SUGN12}}^2}+\frac{1}{\tau_{\mathrm{SUGN3}}^2}\right)^{-1/2} \tag{12}$$

$$\tau_{\mathrm{SUGN12}}=\left(\sum_{a=1}^{n_{\mathrm{en}}}\left|\frac{\partial N_a}{\partial t}+\mathbf{u}^h\cdot\nabla N_a\right|\right)^{-1} \tag{13}$$

$$\tau_{\mathrm{SUGN3}}=\frac{h_{\mathrm{RGN}}^2}{4\nu} \tag{14}$$

$$h_{\mathrm{RGN}}=2\left(\sum_{a=1}^{n_{\mathrm{en}}}|\mathbf{r}\cdot\nabla N_a|\right)^{-1} \tag{15}$$

$$\mathbf{r}=\frac{\nabla\|\mathbf{u}^h\|}{\|\nabla\|\mathbf{u}^h\|\|} \tag{16}$$

$$\tau_{\mathrm{PSPG}}=\tau_{\mathrm{SUPG}} \tag{17}$$

and in [53]:

$$\nu_{\mathrm{LSIC}}=\tau_{\mathrm{SUPG}}\ \|\mathbf{u}^h-\mathbf{v}^h\|^2 \tag{18}$$

where $n_{\mathrm{en}}$ is the number of (space–time) element nodes and $N_a$ is the space–time shape function associated with the space–time node $a$. As an alternative to the construction of $\tau_{\mathrm{SUPG}}$ as given by Equations (12)–(13), we proposed in [53] the option of constructing $\tau_{\mathrm{SUPG}}$ based on separate definitions for the advection-dominated and transient-dominated limits:

$$\tau_{\mathrm{SUPG}}=\left(\frac{1}{\tau_{\mathrm{SUGN1}}^2}+\frac{1}{\tau_{\mathrm{SUGN2}}^2}+\frac{1}{\tau_{\mathrm{SUGN3}}^2}\right)^{-1/2} \tag{19}$$

$$\tau_{\mathrm{SUGN1}}=\left(\sum_{a=1}^{n_{\mathrm{en}}}|(\mathbf{u}^h-\mathbf{v}^h)\cdot\nabla N_a|\right)^{-1} \tag{20}$$



DOI: 10.1002/fld

$$\tau_{\mathrm{SUGN2}} = \frac{\Delta t}{2} \tag{21}$$

where $\mathbf{v}^h$ is the mesh velocity. It was noted in [53] that separating $\tau_{\mathrm{SUGN12}}$ into its advection-dominated and transient-dominated components as given by Equations (20)–(21) is equivalent to excluding the $(\partial N_a/\partial t|_\xi)$ part of $(\partial N_a/\partial t)$ in Equation (13), making that the definition for $\tau_{\mathrm{SUGN1}}$, and accounting for $(\partial N_a/\partial t|_\xi)$ in the definition for $\tau_{\mathrm{SUGN2}}$ given by Equation (21). Here, $\xi$ is the vector of element (parent–domain) coordinates. For more ways of calculating $\tau_{\mathrm{SUPG}}$, $\tau_{\mathrm{PSPG}}$ and $\nu_{\mathrm{LSIC}}$, see [19, 62–64]. References [19, 63, 64] also include the discontinuity-capturing directional dissipation stabilization, which was introduced as an alternative to the LSIC stabilization.

*Remark 1*

As an alternative to how the SUPG test function is defined in Equation (10), we proposed in [53] the SUPG test function option of replacing $(\partial \mathbf{w}^h/\partial t + \mathbf{u}^h \cdot \nabla \mathbf{w}^h)$ with $((\mathbf{u}^h - \mathbf{v}^h) \cdot \nabla \mathbf{w}^h)$. This replacement is equivalent to excluding the $(\partial \mathbf{w}^h/\partial t|_\xi)$ part of $(\partial \mathbf{w}^h/\partial t)$. In [53], we called this option 'WTSE', and the option where the $(\partial \mathbf{w}^h/\partial t|_\xi)$ term is active 'WTSA'.

*Remark 2*

With the function spaces defined in the paragraph preceding Equation (10), for each space–time slab velocity and pressure assume double unknown values at each spatial node. One value corresponds to the lower end of the slab, and the other one to the upper end. In [53], the option of using double unknown values at a spatial node is called 'DV' for velocity and 'DP' for pressure. In this case, as it was pointed out in [53], we use two integration points over the time interval of the space–time slab, and this time-integration option is called 'TIP2'. This version of the DSD/SST formulation, with the options set DV, DP and TIP2, is called 'DSD/SST-DP'.

*Remark 3*

We proposed in [53] the option of using, for each space–time slab, a single unknown pressure value at each spatial node and called that option 'SP'. With this, we proposed in [53] another version of the DSD/SST formulation, where the options set is DV, SP and TIP2, and called that version 'DSD/SST-SP'. Because the number of unknown pressure values is halved, the computational cost is reduced substantially.

*Remark 4*

To reduce the computational cost further, we proposed in [53] the option of using only one integration point over the time interval of the space–time slab and called that time-integration option 'TIP1'. With that, we proposed in [53] a third version of the DSD/SST formulation, where the options set is DV, SP and TIP1, and called that version 'DSD/SST-TIP1'.

*Remark 5*

As a third way of reducing the computational cost, we proposed in [53] the option of using, for each space–time slab, a single unknown velocity value at each spatial node and called that option 'SV'. In the SV option of the two parts of Equation (10), the one generated by $(\mathbf{w}^h)_n^+$ is removed, and we explicitly set $(\mathbf{u}^h)_n^+ = (\mathbf{u}^h)_n^-$, which makes the velocity field continuous in time. On the basis of SV option, we proposed in [53] a fourth version of the DSD/SST formulation, where the options set is SV, SP and TIP1, and called that version 'DSD/SST-SV'. With this version of the DSD/SST formulation, we proposed in [53] to use the SUPG test function option WTSE.



DOI: 10.1002/fld

*Remark 6*
As it was pointed out in [53], versions DSD/SST-TIP1 and DSD/SST-SV render the DSD/SST versions used earlier obsolete (see Remark 8 in [53]).

### *3.2. Semi-discrete formulation of structural mechanics*

Using $\mathbf{y}^h$ and $\mathbf{w}^h$ from appropriately defined trial and test function spaces, respectively, the semi-discrete finite element formulation of the structural mechanics equations (see [16, 65, 66]) is expressed as

$$\int_{\Omega_0^s} \mathbf{w}^h \cdot \rho^s \frac{\mathrm{d}^2\mathbf{y}^h}{\mathrm{d}t^2}\,\mathrm{d}\Omega^s + \int_{\Omega_0^s} \mathbf{w}^h \cdot \eta\rho^s \frac{\mathrm{d}\mathbf{y}^h}{\mathrm{d}t}\,\mathrm{d}\Omega^s + \int_{\Omega_0^s} \delta\mathbf{E}^h : \mathbf{S}^h\,\mathrm{d}\Omega^s$$
$$= \int_{\Omega_t^s} \mathbf{w}^h \cdot (\mathbf{t}^h + \rho^s\mathbf{f}^s)\,\mathrm{d}\Omega^s \tag{22}$$

The fluid mechanics forces acting on the structure are represented by vector $\mathbf{t}^h$. The above formulation is for structures represented by a membrane model (extending the formulation to structures represented by a 3D continuum model is described in Section 3.3). The left-hand side terms of Equation (22) are referred to in the original configuration and the right-hand side terms in the deformed configuration at time $t$. From this formulation at each time step we obtain a nonlinear system of equations. In solving that nonlinear system with an iterative method, we use an incremental form (see [15, 16, 65, 66]), which is expressed as

$$\left[\frac{\mathbf{M}}{\beta\Delta t^2} + \frac{(1-\alpha)\gamma\mathbf{C}}{\beta\Delta t} + (1-\alpha)\mathbf{K}\right]\Delta\mathbf{d}^i = \mathbf{R}^i \tag{23}$$

Here $\mathbf{M}$ is the mass matrix, $\mathbf{C}$ is the damping matrix, $\mathbf{K}$ is the consistent tangent matrix associated with the internal elastic forces, $\mathbf{R}^i$ is the residual vector at the $i$th iteration and $\Delta\mathbf{d}^i$ is the $i$th increment in the nodal displacements vector $\mathbf{d}$. For spatially constant $\eta$, the damping matrix can be expressed as $\mathbf{C} = \eta\mathbf{M}$. All of the terms known from the previous iteration are lumped into the residual vector $\mathbf{R}^i$. The parameters $\alpha, \beta, \gamma$ are part of the Hilber–Hughes–Taylor [67] scheme, which is the time-integration technique used here.

### *3.3. Stabilized space–time fluid–structure interaction (SSTFSI) technique*

The SSTFSI technique was introduced in [53], where it was described based on the finite element formulations given by Equations (10) and (22), with a slight change in notation and with a clarification of how the fluid–structure interface conditions are handled. In that notation subscripts 1 and 2 refer to fluid and structure, respectively. Furthermore, while subscript I refers to the fluid–structure interface, subscript E refers to 'elsewhere' in the fluid and structure domains or boundaries. Here we repeat from [53] the equations representing the SSTFSI technique:

$$\int_{Q_n} \mathbf{w}_{1\mathrm{E}}^h \cdot \rho\left(\frac{\partial\mathbf{u}^h}{\partial t} + \mathbf{u}^h \cdot \nabla\mathbf{u}^h - \mathbf{f}^h\right)\mathrm{d}Q + \int_{Q_n} \boldsymbol{\varepsilon}(\mathbf{w}_{1\mathrm{E}}^h) : \boldsymbol{\sigma}(p^h, \mathbf{u}^h)\,\mathrm{d}Q$$
$$- \int_{(P_n)_h} \mathbf{w}_{1\mathrm{E}}^h \cdot \mathbf{h}_{1\mathrm{E}}^h\,\mathrm{d}P + \int_{Q_n} q_{1\mathrm{E}}^h \nabla\cdot\mathbf{u}^h\,\mathrm{d}Q + \int_{\Omega_n} (\mathbf{w}_{1\mathrm{E}}^h)_n^+ \cdot \rho((\mathbf{u}^h)_n^+ - (\mathbf{u}^h)_n^-)\,\mathrm{d}\Omega$$



DOI: 10.1002/fld

$$+\sum_{e=1}^{(n_{\mathrm{el}})_n}\int_{Q_n^e}\frac{1}{\rho}\left[\tau_{\mathrm{SUPG}}\rho\left(\frac{\partial\mathbf{w}_{1\mathrm{E}}^h}{\partial t}+\mathbf{u}^h\cdot\nabla\mathbf{w}_{1\mathrm{E}}^h\right)+\tau_{\mathrm{PSPG}}\nabla q_{1\mathrm{E}}^h\right]\cdot[Ł(p^h,\mathbf{u}^h)-\rho\mathbf{f}^h]\,\mathrm{d}Q$$

$$+\sum_{e=1}^{(n_{\mathrm{el}})_n}\int_{Q_n^e}\nu_{\mathrm{LSIC}}\nabla\cdot\mathbf{w}_{1\mathrm{E}}^h\rho\nabla\cdot\mathbf{u}^h\,\mathrm{d}Q=0 \tag{24}$$

$$\int_{Q_n}q_{1\mathrm{I}}^h\nabla\cdot\mathbf{u}^h\,\mathrm{d}Q+\sum_{e=1}^{(n_{\mathrm{el}})_n}\int_{Q_n^e}\frac{1}{\rho}[\tau_{\mathrm{PSPG}}\nabla q_{1\mathrm{I}}^h]\cdot[Ł(p^h,\mathbf{u}^h)-\rho\mathbf{f}^h]\,\mathrm{d}Q=0 \tag{25}$$

$$\int_{(\Gamma_{1\mathrm{I}})_{\mathrm{REF}}}(\mathbf{w}_{1\mathrm{I}}^h)_{n+1}^-\cdot((\mathbf{u}_{1\mathrm{I}}^h)_{n+1}^--\mathbf{u}_{2\mathrm{I}}^h)\,\mathrm{d}\Gamma=0 \tag{26}$$

$$\int_{(P_n)_h}(\mathbf{w}_{1\mathrm{I}}^h)_{n+1}^-\cdot\mathbf{h}_{1\mathrm{I}}^h\,\mathrm{d}P=-\int_{(P_n)_h}(\mathbf{w}_{1\mathrm{I}}^h)_{n+1}^-\cdot p\mathbf{n}\,\mathrm{d}P+\int_{Q_n}2\mu\boldsymbol{\varepsilon}((\mathbf{w}_{1\mathrm{I}}^h)_{n+1}^-):\boldsymbol{\varepsilon}(\mathbf{u})\,\mathrm{d}Q$$
$$+\int_{Q_n}(\mathbf{w}_{1\mathrm{I}}^h)_{n+1}^-\cdot\nabla\cdot(2\mu\boldsymbol{\varepsilon}(\mathbf{u}))\,\mathrm{d}Q \tag{27}$$

$$\int_{(\Omega_{2I})_{\mathrm{REF}}}\mathbf{w}_{2\mathrm{I}}^h\cdot(\mathbf{h}_{2\mathrm{I}}^h+(\mathbf{h}_{1\mathrm{I}}^h)_{\mathrm{A}}+(\mathbf{h}_{1\mathrm{I}}^h)_{\mathrm{B}})\,\mathrm{d}\Omega=0 \tag{28}$$

$$\int_{(\Omega_2)_0}\mathbf{w}_2^h\cdot\rho_2\frac{\mathrm{d}^2\mathbf{y}^h}{\mathrm{d}t^2}\,\mathrm{d}\Omega+\int_{(\Omega_2)_0}\mathbf{w}_2^h\cdot\eta\rho_2\frac{\mathrm{d}\mathbf{y}^h}{\mathrm{d}t}\,\mathrm{d}\Omega+\int_{(\Omega_2)_0}\delta\mathbf{E}^h:\mathbf{S}^h\,\mathrm{d}\Omega$$
$$=\int_{\Omega_2}\mathbf{w}_2^h\cdot\rho_2\mathbf{f}_2^h\,\mathrm{d}\Omega+\int_{\Omega_{2\mathrm{E}}}\mathbf{w}_{2\mathrm{E}}^h\cdot\mathbf{h}_{2\mathrm{E}}^h\,\mathrm{d}\Omega+\int_{\Omega_{2\mathrm{I}}}\mathbf{w}_{2\mathrm{I}}^h\cdot\mathbf{h}_{2\mathrm{I}}^h\,\mathrm{d}\Omega \tag{29}$$

Here, $(\Gamma_{2\mathrm{I}})_{\mathrm{REF}}$ and $(\Omega_{2\mathrm{I}})_{\mathrm{REF}}$ represent some reference configurations of $\Gamma_{2\mathrm{I}}$ and $\Omega_{2\mathrm{I}}$, respectively. In reconciling the slightly modified notation used here with the notation used in Equations (10) and (22), we note that $\rho_2=\rho^{\mathrm{s}}$, $\mathbf{f}_2^h=\mathbf{f}^{\mathrm{s}}$, $(\Omega_2)_0=\Omega_0^{\mathrm{s}}$, $\Omega_2=\Omega_t^{\mathrm{s}}$, and $\Omega_{2\mathrm{I}}$ and $\Omega_{2\mathrm{E}}$ indicate the partitions of $\Omega_2$ corresponding to the interface and 'elsewhere'. We also note that $\mathbf{h}_{2\mathrm{I}}^h=\mathbf{t}^h$, and $(\mathbf{h}_{1\mathrm{I}}^h)_{\mathrm{A}}$ and $(\mathbf{h}_{1\mathrm{I}}^h)_{\mathrm{B}}$ represent the values of $\mathbf{h}_{1\mathrm{I}}^h$ associated with the fluid surfaces above and below the membrane structure. The symbol $\mathbf{h}_{2\mathrm{E}}^h$ denotes the prescribed external forces acting on the structure in $\Omega_{2\mathrm{E}}$, which is separate from $\mathbf{f}_2^h$. In this formulation, $(\mathbf{u}_{1\mathrm{I}}^h)_{n+1}^-$, $\mathbf{h}_{1\mathrm{I}}^h$ and $\mathbf{h}_{2\mathrm{I}}^h$ (the fluid velocity, fluid stress and structural stress at the interface) are treated as separate unknowns, and Equations (26), (27) and (28) can be seen as equations corresponding to these three unknowns, respectively. The structural displacement rate at the interface, $\mathbf{u}_{2\mathrm{I}}^h$, is derived from $\mathbf{y}^h$.

The formulation above is based on allowing for cases when the fluid and structure meshes at the interface are not identical. If they are identical, as it was pointed out in [53], the same formulation can still be used. Also as it was pointed out in [53], if the structure is represented by a 3D continuum model instead of a membrane model, the formulation above would still be applicable if the domain integrations over $\Omega_{2\mathrm{E}}$ and $\Omega_{2\mathrm{I}}$ in the last two terms of Equation (29) are converted to boundary integrations over $\Gamma_{2\mathrm{E}}$ and $\Gamma_{2\mathrm{I}}$. In such cases, $\mathbf{h}_{2\mathrm{E}}^h$ would represent the prescribed forces acting 'elsewhere' on the surface of the structure.



DOI: 10.1002/fld

It was noted in [53] that, for constant viscosity, the term $\nabla \cdot (2\mu\varepsilon(\mathbf{u}))$ in Equation (27) vanishes for tetrahedral elements and in most cases can be neglected for hexahedral elements. It was further noted in [53] that the same statement can be made also in the context of that term being a part of the expression $Ł(p^h, \mathbf{u}^h)$ appearing in Equations (24) and (25).

*Remark 7*
In [53], the versions of the SSTFSI method corresponding to the DSD/SST-DP, DSD/SST-SP, DSD/SST-TIP1 and DSD/SST-SV formulations (see Remarks 2–5) were called 'SSTFSI-DP', 'SSTFSI-SP', 'SSTFSI-TIP1' and 'SSTFSI-SV', respectively.

*Remark 8*
As it was pointed out in [53], versions SSTFSI-TIP1 and SSTFSI-SV render the SSTFSI versions used earlier obsolete (see Remark 12 in [53]).

### *3.4. Mesh update methods*

The mesh update methods, and related techniques, developed by the T★AFSM to be used in conjunction with the DSD/SST formulation were described in a Section in [53]. The section includes references to a number of articles where these methods and techniques were described in detail (see [11, 25, 36, 50, 51, 68–74]), as well as references to related methods developed by other researchers (see [75–77]).

### *3.5. Solution of the fully discretized coupled equations*

Full discretization of the FSI formulation described in Section 3.3 leads to coupled, nonlinear equation systems that need to be solved at every time step. The techniques developed by the T★AFSM for that purpose were described in a section in [53]. The section includes references to a number of articles where related techniques were described in detail (see [22, 29, 30, 52, 63, 78–81]), as well as references to related methods developed by other researchers (see [82–84]).

### *3.6. Segregated equation solvers*

The iterative solution approaches needed in arterial fluid mechanics computations, especially with the long computational domains inherent to such computations, are expected to benefit significantly from advanced segregated equation solvers. A recent demonstration of this potential can be found in [85, 86]. Segregated equation solver techniques recently developed by the T★AFSM for FSI computations were described in a section in [53]. The section includes references to earlier articles describing related techniques and applications (see [11, 46, 47, 87–90]).

## 4. ESTIMATED ZERO-PRESSURE ARTERIAL GEOMETRY

In [8], what was used as the arterial geometries corresponding to zero blood pressure were close approximations to patient-specific image-based geometries extracted from computed tomography models. Here, we take a more realistic approach by recognizing that such image-based geometries should be used as arterial geometries corresponding to time-averaged pressure values. We use a rudimentary technique to estimate the zero-pressure arterial geometry. This concept was first introduced in [57].



DOI: 10.1002/fld

To explain the concept more, we use as example one of the test cases computed in [8]. The test case was 'middle cerebral artery with aneurysm—single-artery segment', with normal blood pressure (NBP) in an artery segment with uniform wall thickness. The arterial geometry used was a close approximation to the patient-specific image-based geometry used in [7]. The geometry used in [7] was extracted from the computed tomography model of a segment of the middle cerebral artery of a 57-year-old male with aneurysm. The nominal value of the arterial diameter was 3.0 mm, with an assumed wall thickness of 0.3 mm. In the test computations reported in [8], the image-based geometry (with nominal diameter 3.0 mm) was used as the arterial geometry corresponding to zero blood pressure. However, it is more realistic to use that image-based geometry as the arterial geometry corresponding to the time-averaged value of the blood pressure. Given that arterial geometry at the time-averaged pressure value, an estimated arterial geometry corresponding to zero blood pressure needs to be constructed.

We estimate the zero-pressure arterial geometry in conjunction with an arterial structural model based on the continuum element made of hyperelastic (Fung) material. We use an estimated configuration for the zero-pressure geometry and try different values for the zero-pressure wall thickness until the arterial geometry we obtain with the time-averaged pressure value has the same diameter and wall thickness as the approximate image-based geometry. We realize that we are matching only two of the parameters that represent the image-based geometry, but considering that a full matching would be quite challenging, we feel that our rudimentary technique is a good start in estimating the zero-pressure arterial geometry. The first test computation we report in Section 8, namely 'middle cerebral artery with aneurysm—single-artery segment', is based on this concept.

## 5. FLUID AND STRUCTURE PROPERTIES AND BOUNDARY CONDITIONS

### *5.1. Fluid and structure properties*

As it was done for the computations reported in [1, 2, 4, 5, 7, 10], the blood is assumed to behave like a Newtonian fluid (see Section 2.1). The density and kinematic viscosity are set to $1000\,\mathrm{kg\,m^{-3}}$ and $4.0\times10^{-6}\,\mathrm{m^2\,s^{-1}}$. The material density of the arterial wall is known to be close to that of the blood and therefore set to $1000\,\mathrm{kg\,m^{-3}}$. The stiffness values used for the arteries are comparable with those used in [1, 2, 4, 5, 7, 10], where the values used were determined (see [7]) by comparison with experimental values. The stiffness value used in each test case is given in the individual description of that test case. Arteries are surrounded by tissues, and we expect those tissues to have a damping effect on the structural dynamics of the arteries. Therefore, we add a mass-proportional damping, which also helps in removing the high-frequency modes of the structural deformation. The damping coefficient $\eta$ used in each case is given in the individual description of that case.

### *5.2. Boundary conditions*

In all the test cases computed, we have a single inflow boundary where we specify the velocity profile as a function of time. The profile is similar to the one obtained by using the Womersley solution of a pulsating flow [91]. At the outflow boundaries, we specify traction boundary conditions. In test cases with two outflow boundaries, we specify the same condition for both. The traction boundary condition is based on the pressure profile applicable to the case computed. The pressure profile, as a function of time, is obtained from an approximate solution [4] of the Windkessel model [92]. The parameters in the Windkessel model are set in such a way that the



DOI: 10.1002/fld

range for the pressure profile is approximately from 80 to 120 mmHg for NBP and from 100 to 170 mmHg for high blood pressure (HBP). On the arterial walls, we specify no-slip boundary conditions for the flow. In the structural mechanics part, as a boundary condition at the ends of the arteries, for computations with the membrane element we set the displacement to zero. For computations with the continuum element, we set the normal component of the displacement to zero.

## 6. SIMULATION SEQUENCE

In most of the simulations carried out by the T★AFSM, the FSI computations are preceded by a set of pre-FSI computations that provide us a good starting point for the FSI computations. These pre-FSI computations include the fluid-only and structure-only computations. We have two options for the pre-FSI generation of the fluid mesh. We can generate it by starting with a mesh corresponding to the initial shape of the structure and updating it as the structure-only computation proceeds, or generate it after the structure-only computation is completed. We built two simulation sequences that were used in the computations reported here. Our experience with the first one helped us design the second one.

### *6.1. Fluid→structure→FSI (F→S→FSI) sequence*

*Step 1*: Generate the fluid and structure meshes based on the shape of the unstressed structure.
*Step 2*: Compute a developed flow field while holding the structure rigid.

- The outflow traction is set to a value close to 80 mmHg for NBP and 100 mmHg for HBP.
- The inflow velocity is set to a value corresponding to the outflow traction.

*Step 3*: Compute the structural deformation, with the fluid stresses at the interface held steady at their values from Step 2, and simultaneously update the fluid mesh.

- Structural deformation can be determined with a steady-state computation or a time-dependent computation that eventually yields a steady-state solution.
- For the steady-state computation, $\Delta t \to \infty$ and $\alpha = 0$ in Equation (23) in [53], the number of time steps is 1, and the initial displacement, velocity and acceleration are set to zero.
- The mesh quality obtained with the time-dependent computation is better than the one obtained with the steady-state computation.

*Step 4*: Compute the FSI with the inflow and outflow conditions held steady at the values used in Step 2.

- Sometimes, to prevent a sudden increase in the structural acceleration at the start of this step, it may be necessary to begin with an increased structural mass that would later be decreased back to its actual value. An unrealistically large acceleration can initiate an instability that is subsequently magnified.

*Step 5*: Compute the FSI with the inflow and outflow conditions pulsating.

### *6.2. Structure→fluid→FSI (S→F→FSI) sequence*

Analysis of the results obtained with the F→S→FSI sequence revealed that the fluid pressure is spatially almost uniform. Even when the outflow traction is pulsating, although the pressure



DOI: 10.1002/fld

changes as a function of time, spatially it remains nearly uniform. The S → F → FSI sequence was built based on these considerations.

*Step 1*: Generate the structure mesh based on the shape of the unstressed structure.

*Step 2*: Compute the structural deformation with a uniform fluid pressure held steady at a value close to 80 mmHg for NBP and 100 mmHg for HBP.

- The structural deformation can be computed, as how it was done at Step 3 of the F → S → FSI sequence, with a steady-state computation or a time-dependent computation that eventually yields a steady-state solution.

*Step 3*: Generate the fluid mesh based on the shape of the deformed structure.

*Step 4*: Compute a developed flow field while holding the structure from Step 2 rigid.

- The outflow traction is set to a value close to 80 mmHg for NBP and 100 mmHg for HBP.
- The inflow velocity is set to a value corresponding to the outflow traction.

*Step 5*: Continue from Step 4 of the F → S → FSI sequence.

## 7. SEQUENTIALLY COUPLED ARTERIAL FSI TECHNIQUE

The SCAFSI technique was first proposed in [58] as an approximate FSI approach in arterial fluid mechanics. In the SCAFSI technique, first we compute a 'reference' (i.e. 'base') arterial deformation as a function of time, driven only by the blood pressure, which is given as a function of time by specifying the pressure profile in a cardiac cycle. Then, we compute a sequence of updates involving mesh motion, fluid dynamics calculations and recomputing the arterial deformation.

*Step 1*: Compute the 'reference' arterial displacement $(\mathbf{Y}_R)_n$ $(n=1,2,\ldots,n_{ts})$, driven only by the blood pressure $p_R(t)$, which is given by specifying the pressure profile in a cardiac cycle. In moving from time level $n$ to $n+1$, we propose the following options for the predictor $((\mathbf{Y}_R)_{n+1})^0$: $(\mathbf{Y}_R)_n$, $2(\mathbf{Y}_R)_n-(\mathbf{Y}_R)_{n-1}$, $3(\mathbf{Y}_R)_n-3(\mathbf{Y}_R)_{n-1}+(\mathbf{Y}_R)_{n-2}$ and $(\mathbf{Y}_R)_n+((\mathbf{Y}_R)_n-(\mathbf{Y}_R)_{n-1})/(p_R(t_n)-p_R(t_{n-1}))(p_R(t_{n+1})-p_R(t_n))$. Let $(\mathbf{P}_R)_n$ denote the vector of nodal values of pressure where every nodal value is equal to $p_R(t_n)$, and let $(\mathbf{H}_R)_n$ denote the interface stress associated with that.

*Step 2*: Given the displacements from Step 1, compute the 'reference' mesh motion $(\mathbf{X}_R)_n$ $(n=1,2,\ldots,n_{ts})$. At each time level $n+1$, in computing $(\mathbf{X}_R)_{n+1}$, as the initial guess $((\mathbf{X}_R)_{n+1})^0$, we consider the option $((\mathbf{X}_R)_{n+1})^0=\mathbf{0}$ and the options we had for $((\mathbf{Y}_R)_{n+1})^0$ in Step 1.

*Step 3*: Given the displacements and mesh motion from Steps 1 and 2, for zero-stress conditions at the outflow boundaries, compute the time-dependent flow field and the corresponding interface stress vector $(\mathbf{H}_1)_n$ $(n=1,2,\ldots,n_{ts})$. At each time level $n+1$, in computing the flow field, as the initial guess for pressure, we consider the following options for $((\mathbf{P}_1)_{n+1})^0$: $(\mathbf{P}_1)_n$, $2(\mathbf{P}_1)_n-(\mathbf{P}_1)_{n-1}$ and $3(\mathbf{P}_1)_n-3(\mathbf{P}_1)_{n-1}+(\mathbf{P}_1)_{n-2}$. To enhance the stability of the computation in Step 4, we propose to smoothen $(\mathbf{H}_1)_n$ with the following time-averaging formula:

$$\begin{aligned}(\mathbf{H}_1)_n \leftarrow\ & \omega_0(\mathbf{H}_1)_n \\ & +\omega_{\pm1}((\mathbf{H}_1)_{n+1}+(\mathbf{H}_1)_{n-1})+\omega_{\pm2}((\mathbf{H}_1)_{n+2}+(\mathbf{H}_1)_{n-2}) \\ & +\omega_{\pm3}((\mathbf{H}_1)_{n+3}+(\mathbf{H}_1)_{n-3})+\omega_{\pm4}((\mathbf{H}_1)_{n+4}+(\mathbf{H}_1)_{n-4})\end{aligned} \tag{30}$$



DOI: 10.1002/fld

For the time-averaging weights, we propose the options $(\omega_0, \omega_{\pm1}, \omega_{\pm2}, \omega_{\pm3}, \omega_{\pm4}) = \frac{1}{9}(3,2,1,0,0)$, $\frac{1}{16}(4,3,2,1,0)$ and $\frac{1}{25}(5,4,3,2,1)$. Now the total interface stress is $\mathbf{H}_n = (\mathbf{H}_R)_n + (\mathbf{H}_1)_n$.

*Step 4*: With the updated interface stresses from Step 3, compute the updated arterial displacement $\mathbf{Y}_n$ $(n = 1, 2, \ldots, n_{ts})$. At each time level $n+1$, in computing $\mathbf{Y}_{n+1}$, as the predictor, we propose $(\mathbf{Y}_{n+1})^0 = (\mathbf{Y}_R)_{n+1} + ((\mathbf{Y}_1)_{n+1})^0$. Here the displacement increment is defined as $(\mathbf{Y}_1)_n = \mathbf{Y}_n - (\mathbf{Y}_R)_n$, and based on that definition, for $((\mathbf{Y}_1)_{n+1})^0$ we consider the options we had for $((\mathbf{P}_1)_{n+1})^0$ in Step 3.

*Step 5*: Compute the updated mesh motion $\mathbf{X}_n$ $(n = 1, 2, \ldots, n_{ts})$. At each time level $n+1$, in computing $\mathbf{X}_{n+1}$, as the initial guess $(\mathbf{X}_{n+1})^0$, we consider the options $(\mathbf{X}_{n+1})^0 = \mathbf{0}$ and $(\mathbf{X}_{n+1})^0 = (\mathbf{X}_R)_{n+1} + ((\mathbf{X}_1)_{n+1})^0$. Here the mesh-motion increment is defined as $(\mathbf{X}_1)_n = \mathbf{X}_n - (\mathbf{X}_R)_n$, and based on that definition, for $((\mathbf{X}_1)_{n+1})^0$ we consider the option $((\mathbf{X}_1)_{n+1})^0 = \mathbf{0}$ and the options we had for $((\mathbf{P}_1)_{n+1})^0$ in Step 3.

*Step 6*: Given the displacements and mesh motion from Steps 4 and 5, for zero-stress conditions at the outflow boundaries, compute the time-dependent flow field and the corresponding interface stress vector $(\mathbf{H}_2)_n$ $(n = 1, 2, \ldots, n_{ts})$. At each time level $n+1$, in computing the flow field, as the initial guess for pressure, we consider for $((\mathbf{P}_2)_{n+1})^0$ the options we had for $((\mathbf{P}_1)_{n+1})^0$ in Step 3 and the option $((\mathbf{P}_2)_{n+1})^0 = (\mathbf{P}_1)_{n+1}$. Now the total interface stress is $\mathbf{H}_n = (\mathbf{H}_R)_n + (\mathbf{H}_2)_n$.

## 8. TEST COMPUTATIONS

All computations were carried out in a parallel computing environment using PC clusters. The meshes were generated on a single node of the cluster used. In all cases computed, the fluid and structure meshes are compatible at the fluid–structure interface. All computations were completed without any remeshing. In all cases, the fully discretized, coupled fluid and structural mechanics and mesh-moving equations were solved with the quasi-direct coupling technique (see Section 5.2 in [53]). In solving the linear equation systems involved at every nonlinear iteration, the GMRES search technique [82] was used with a diagonal preconditioner.

### *8.1. Middle cerebral artery with aneurysm—single-artery segment*

The arterial geometry is from [8]. It is a close approximation to the patient-specific image-based geometry used in [7]. The geometry used in [7] was extracted from the computed tomography model of a segment of the middle cerebral artery of a 57-year-old male with aneurysm. The diameter and length of the artery are 3.0 and 15 mm, and the size of the aneurysm is 6 mm. The volumetric inflow rate used is also a close approximation to the one used in [7], which can be found in [4, 5]. More specifically, our inflow profile was generated by digitizing the data published in [4, 5]. The problem geometry and the pulsating inflow velocity profile as a function of time are shown in Figures 1 and 2.

The test computation is carried out for NBP. Figure 3 shows the NBP profile (together with the HBP profile), which was calculated in the way described in Section 5.2. The traction condition at the outflow boundary is based on this pressure profile. The arterial wall is modeled with the continuum element made of hyperelastic (Fung) material. The wall thickness for the artery is 0.3 mm. The Fung material constants $D_1$ and $D_2$ (from [93]) and the penalty Poisson ratio are $2.6447 \times 10^3\,\mathrm{N\,m^{-2}}$, 8.365 and 0.45, respectively.



DOI: 10.1002/fld

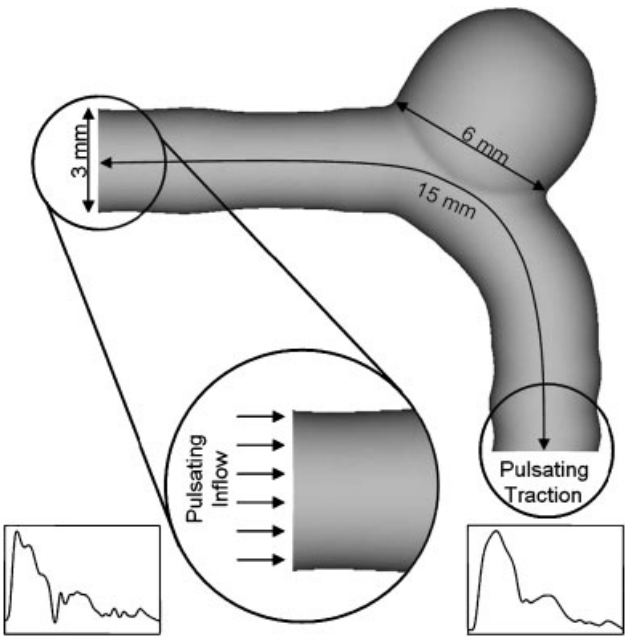


Figure 1. Middle cerebral artery with aneurysm—single-artery segment. Problem geometry.

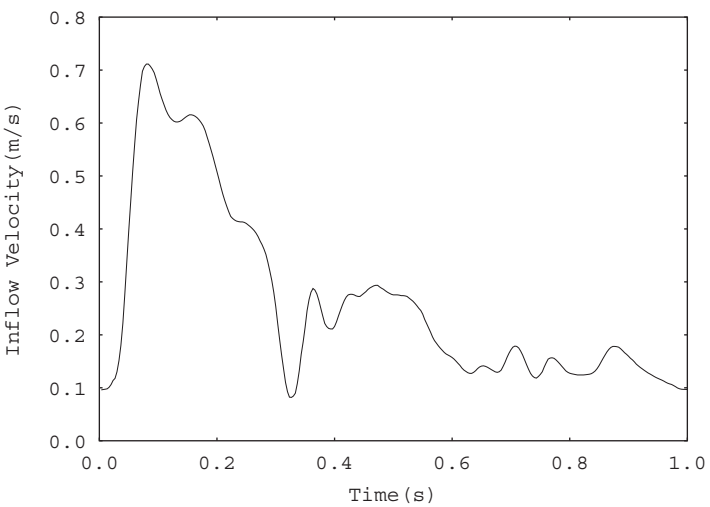


Figure 2. Middle cerebral artery with aneurysm—single-artery segment. Pulsating inflow velocity.

We perform this test computation with the 'estimated zero-pressure arterial geometry' as described in Section 4. The time-averaged value of the blood pressure (see Section 4 for its significance), obtained by averaging over a cardiac cycle, is 91.7 mmHg.



DOI: 10.1002/fld

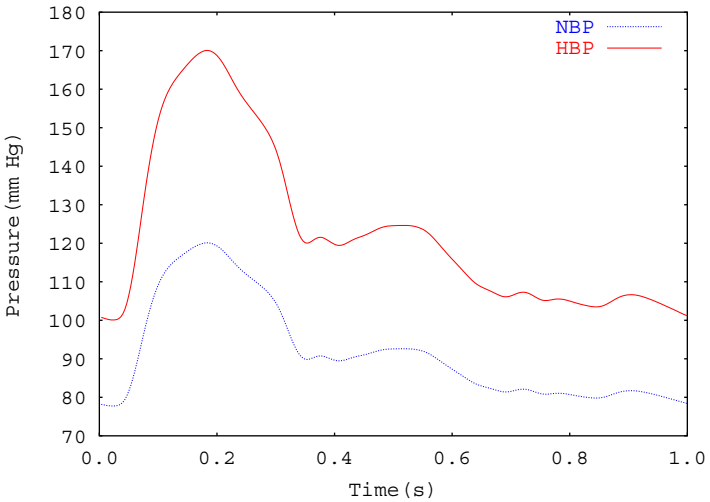


Figure 3. Middle cerebral artery with aneurysm—single-artery segment. Normal and high blood pressure (NBP and HBP) profiles.

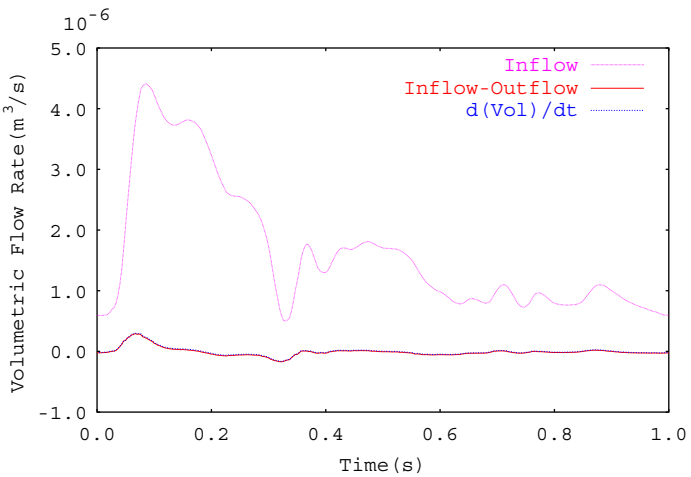


Figure 4. Middle cerebral artery with aneurysm—single-artery segment. Computed with the continuum element made of hyperelastic (Fung) material. Verification of mass balance. Volumetric inflow rate, difference between the volumetric inflow and outflow rates, and rate of change of the artery volume.

The meshes are from [8]. The mesh for the artery consists of 13 332 nodes and 52 944 four-node tetrahedral elements, with 4444 nodes and 8824 three-node triangular elements on the fluid–structure interface. The fluid mechanics mesh contains 9568 nodes and 43 960 four-node tetrahedral elements. The computations are carried out with the SSTFSI-TIP1 technique (see Remarks 4 and 7) and the SUPG test function option WTSA (see Remark 1). The stabilization parameters used are



DOI: 10.1002/fld

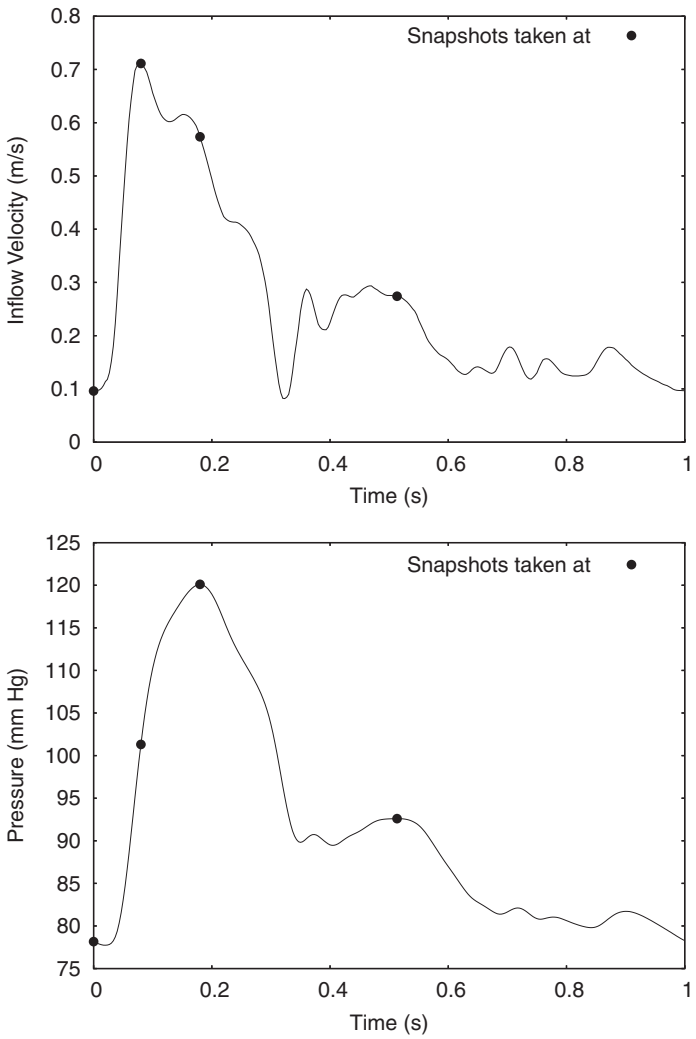


Figure 5. Middle cerebral artery with aneurysm—single-artery segment. Computed with the continuum element made of hyperelastic (Fung) material. Velocity and pressure profiles showing the instants for which the flow field is displayed in Figure 6.

those given by Equations (12)–(18). The damping coefficient $\eta$ is set to $1.5 \times 10^4\,\mathrm{s}^{-1}$. The time-step size is $3.333 \times 10^{-3}\,\mathrm{s}$. The number of nonlinear iterations per time step is 7, and the number of GMRES iterations per nonlinear iteration is 200.

*Remark 9*

We realize that using tetrahedral elements for structures represented by a 3D continuum model may not be the best choice, especially for thin structures. We intend to explore better ways of modeling the arterial walls, including the methods described in [94].



DOI: 10.1002/fld

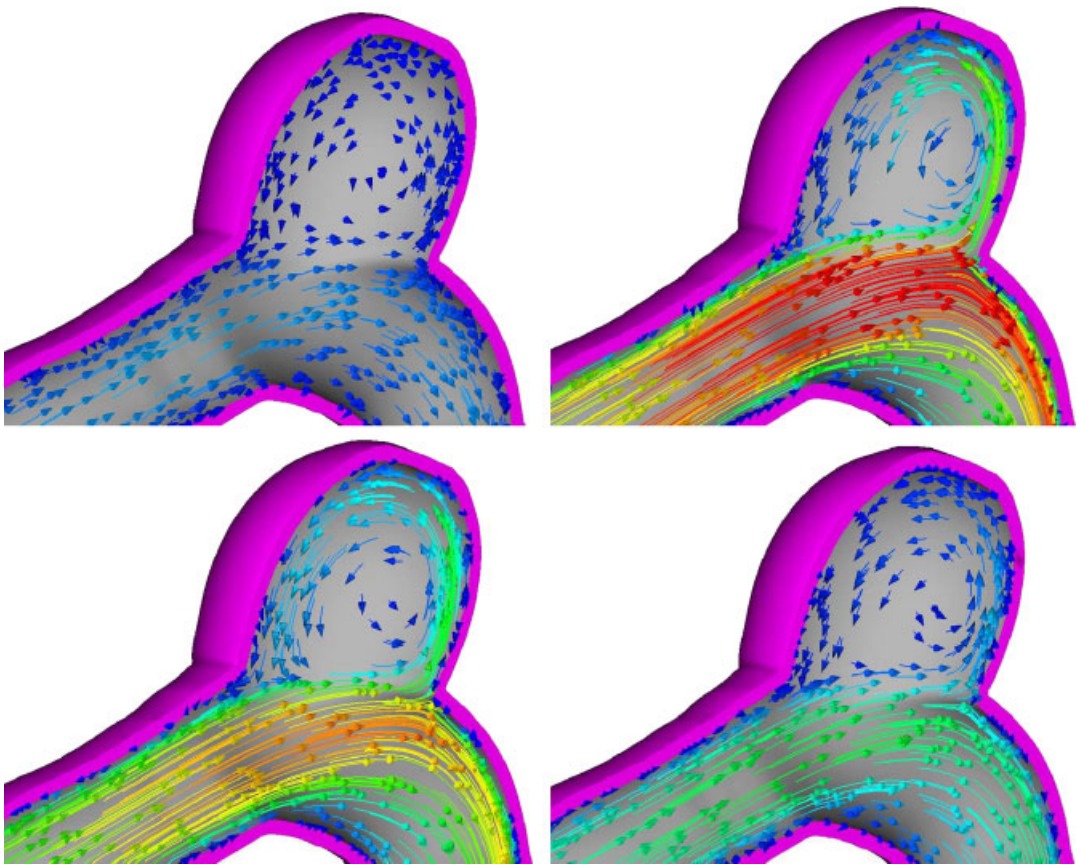

Figure 6. Middle cerebral artery with aneurysm—single-artery segment. Computed with the continuum element made of hyperelastic (Fung) material. Flow field at the instants shown in Figure 5. Velocity vectors colored by magnitude.

We use the 'selective scaling' technique (see Remark 14 in [53]) to dynamically shift the emphasis between the fluid and structure parts. The scales used for the fluid and structure parts at each nonlinear iteration of a time step are given below:

Iteration 1: fluid scale $= 1.00$, structure scale $= 1.0 \times 10^{-1}$.
Iteration 2: fluid scale $= 1.00$, structure scale $= 1.0 \times 10^{-2}$.
Iteration 3: fluid scale $= 1.00$, structure scale $= 1.0 \times 10^{-3}$.
Iteration 4: fluid scale $= 1.00$, structure scale $= 1.0 \times 10^{-4}$.
Iterations 5–7: fluid scale $= 1.00$, structure scale $= 1.0 \times 10^{-5}$.

The $\mathrm{S} \rightarrow \mathrm{F} \rightarrow$ FSI sequence is used in the computation.

We achieve good mass balance. We verify the mass balance by comparing the rate of change for the artery volume and the difference between the volumetric inflow and outflow rates. Figure 4 shows the mass balance. Figures 5 and 6 illustrate the flow field at some specific instants, including



DOI: 10.1002/fld

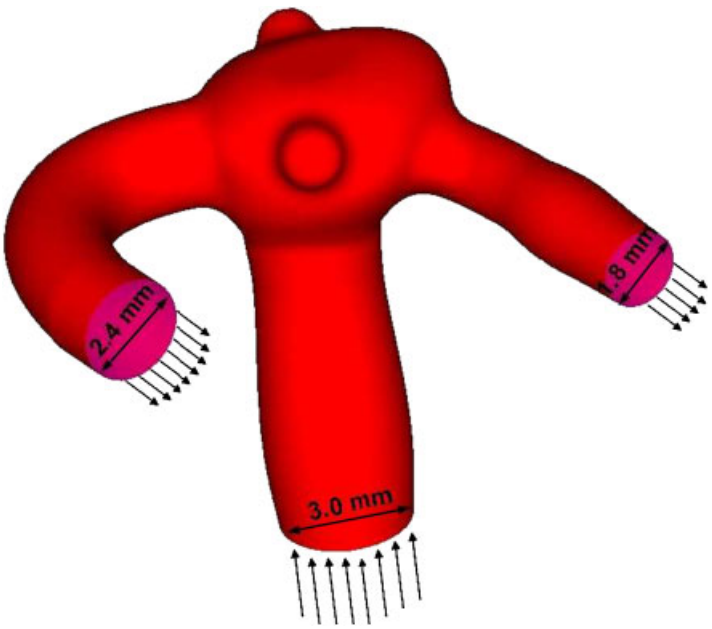


Figure 7. Middle cerebral artery with aneurysm—bifurcating-artery segment. Problem geometry.

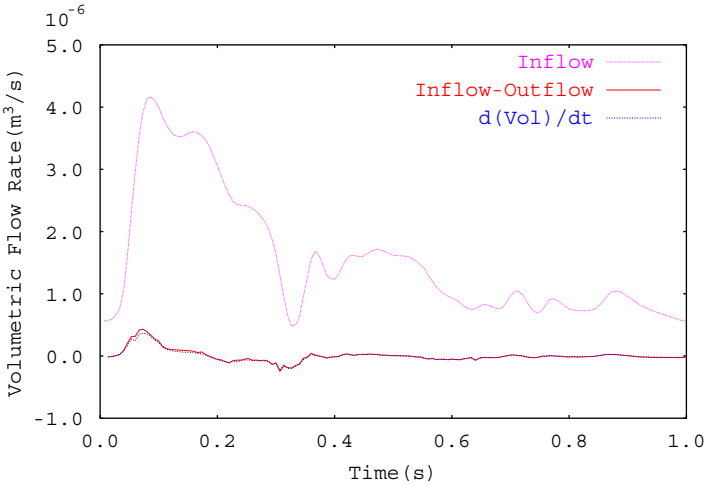


Figure 8. Middle cerebral artery with aneurysm—bifurcating-artery segment. Verification of mass balance. Volumetric inflow rate, difference between the volumetric inflow and outflow rates, and rate of change of the artery volume.

the instants when the inflow velocity is maximum and when the pressure is at its primary and secondary peak values.



DOI: 10.1002/fld

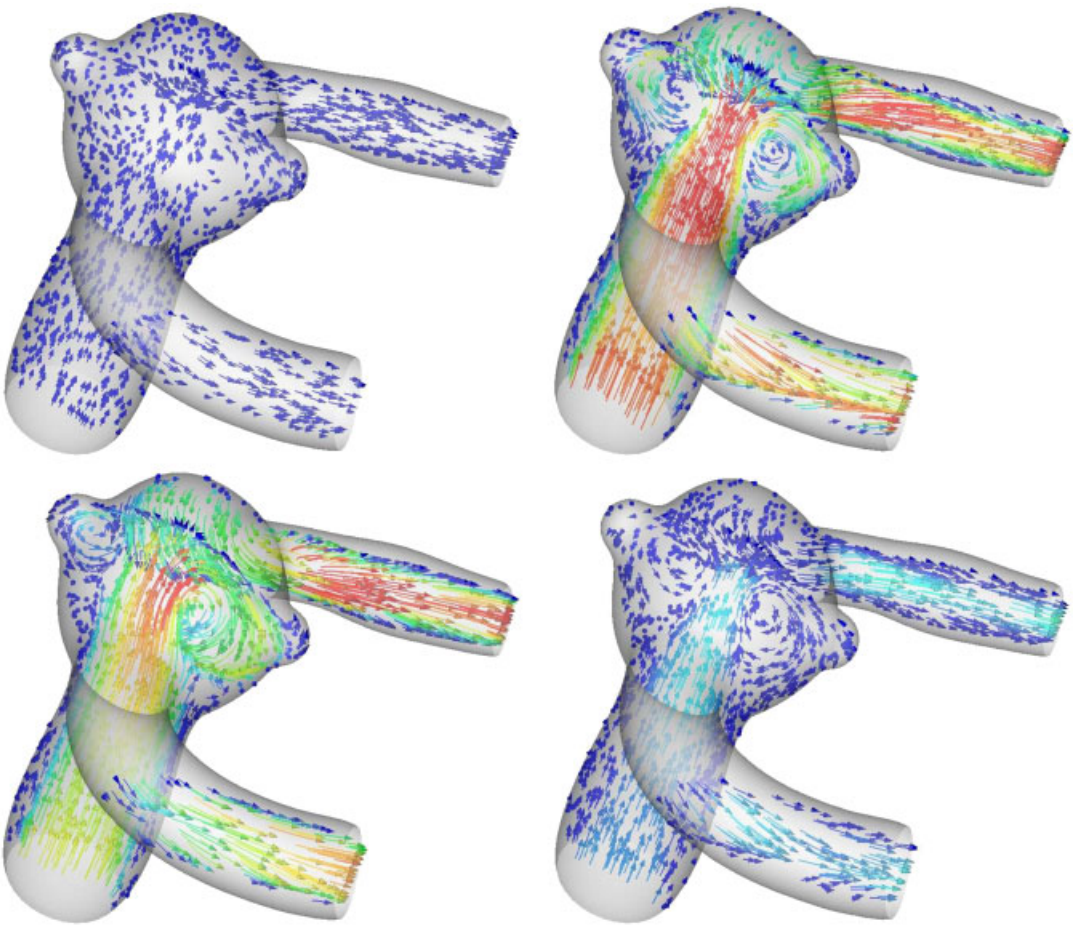

Figure 9. Middle cerebral artery with aneurysm—bifurcating-artery segment. Flow field at approximately the same instants as those marked in Figure 5. Velocity vectors colored by magnitude.

*Remark 10*

We believe that the refinement level of the fluid mechanics meshes we are currently using is sufficient to accurately represent the general trends of the FSI involved in this class of problems. However, more refined meshes are needed for more accurately representing other aspects of these problems, such as the wall shear stress. This will be one of our objectives in our future studies.

### *8.2. Middle cerebral artery with aneurysm—bifurcating-artery segment*

The arterial geometry is from [8]. It is a close approximation to the patient-specific image-based geometry used in [5, 7]. The geometry used in [5, 7] was extracted from the computed tomography model of a segment of the middle cerebral artery of a 59-year-old female with aneurysm. The diameter of the artery segment is 3.0 mm at the inflow, and 2.4 and 1.8 mm at the two outflow ends. The problem geometry is shown in Figure 7. The volumetric inflow rate used is also a close approximation to the one used in [5, 7], which can be found in [4, 5]. The pulsating inflow velocity



DOI: 10.1002/fld

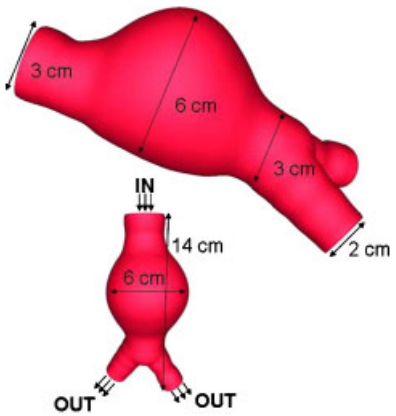


Figure 10. Abdominal aortic aneurysm. Problem geometry.

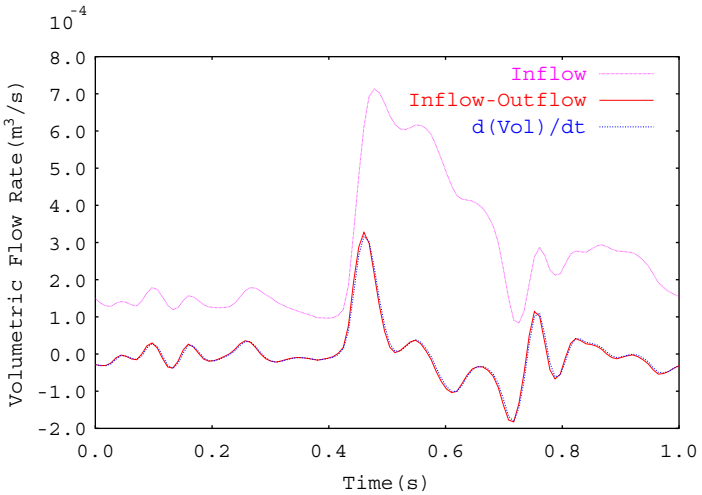


Figure 11. Abdominal aortic aneurysm. Verification of mass balance. Volumetric inflow rate, difference between the volumetric inflow and outflow rates, and rate of change of the artery volume.

profile as a function of time is the same as that shown in Figure 2 in Section 8.1. The traction condition at the outflow boundary is based on the NBP profile shown in Figure 3 in Section 8.1. The structural model is based on the membrane element. The wall thickness, stiffness and Poisson's ratio for the artery are 0.3 mm, $5.0 \times 10^5\,\mathrm{N\,m^{-2}}$ and 0.45, respectively.

The meshes are from [8]. The mesh for the artery consists of 6119 nodes and 12 150 three-node triangular elements. The fluid mechanics mesh contains 14 410 nodes and 66 440 four-node tetrahedral elements. The computation is carried out with the SSTFSI-TIP1 technique (see Remarks 4 and 7) and the SUPG test function option WTSA (see Remark 1). The stabilization parameters used are those given by Equations (12)–(18). The damping coefficient $\eta$ is set to $6.0 \times 10^3\,\mathrm{s^{-1}}$. The time-step size is $6.666 \times 10^{-3}\,\mathrm{s}$. The number of nonlinear iterations per time step is 5, and the number of GMRES iterations per nonlinear iteration is 150. The $\mathrm{F} \rightarrow \mathrm{S} \rightarrow \mathrm{FSI}$



DOI: 10.1002/fld

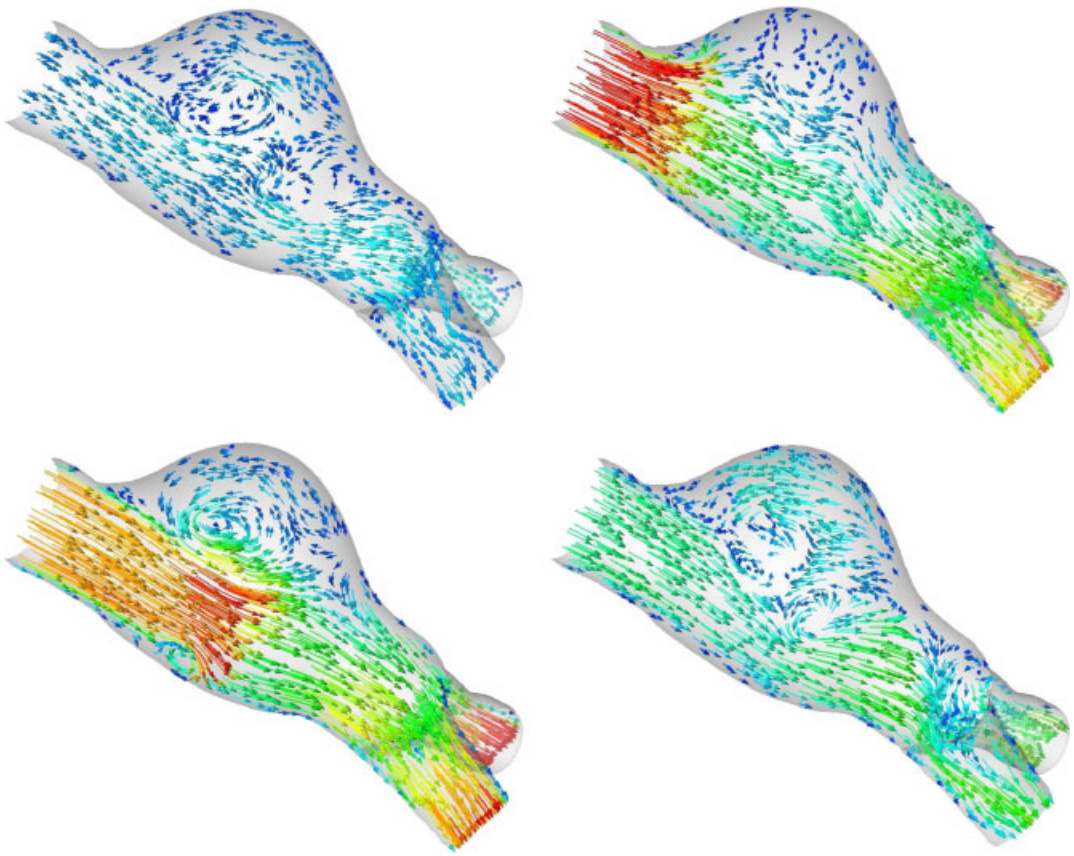

Figure 12. Abdominal aortic aneurysm. Flow field at approximately the same instants as those marked in Figure 5. Velocity vectors colored by magnitude.

sequence is used in the computations. Figure 8 shows the mass balance, and Figure 9 shows the flow field at approximately the same instants as those marked in Figure 5.

### *8.3. Abdominal aortic aneurysm*

The arterial geometry is from [8]. It was created by making use of the image data found in [95, 96], with the arterial diameter and wall thickness coming from [97, 98]. The diameter of the artery segment is 3 cm at the inflow and 2 cm at the two outflow ends. The length is 14 cm and the size of the aneurysm is 6 cm. The problem geometry is shown in Figure 10. The pulsating inflow velocity profile as a function of time is not shown here but has the same form as that shown in Figure 2 in Section 8.1. The minimum and maximum values are 0.13 and $1.13\,\mathrm{m\,s^{-1}}$. The maximum value is based on the data found in [99]. The traction condition at the outflow boundaries is based on a NBP profile calculated in the way described in Section 5.2. That pressure profile is similar to the NBP profile given in Figure 3 in Section 8.1. The structural model is based on the membrane element. The wall thickness, stiffness and Poisson's ratio for the artery are 2.3 mm, $1.0\times10^{6}\,\mathrm{N\,m^{-2}}$ and 0.45, respectively.



DOI: 10.1002/fld

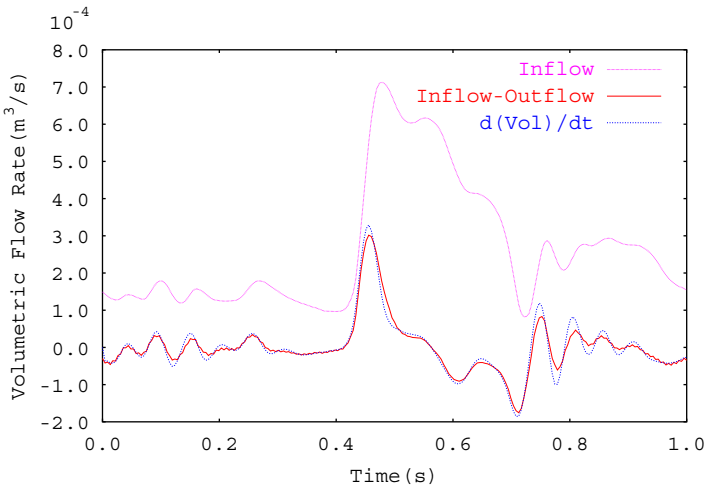


Figure 13. Abdominal aortic aneurysm. Computed with the SCAFSI technique. Verification of mass balance. Volumetric inflow rate, difference between the volumetric inflow and outflow rates and rate of change of the artery volume.

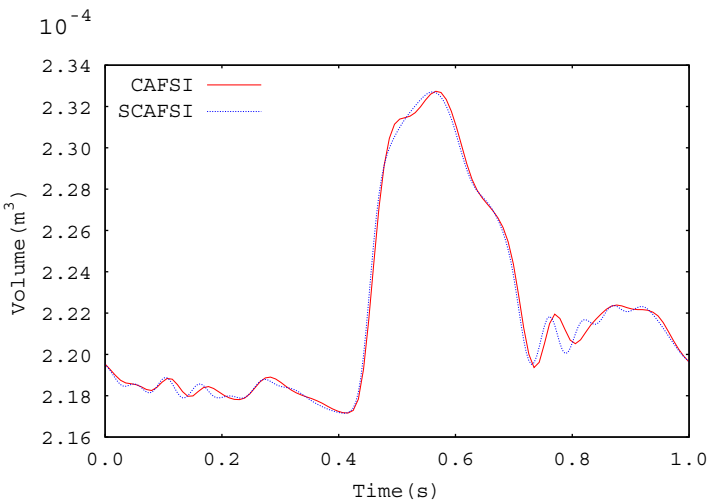


Figure 14. Abdominal aortic aneurysm. Comparison between the SCAFSI and CAFSI techniques. Arterial volume.

The meshes are from [8]. The mesh for the artery consists of 6091 nodes and 12 072 three-node triangular elements. The fluid mechanics mesh contains 49 826 nodes and 295 687 four-node tetrahedral elements. The computations are carried out with the SSTFSI-SV technique (see Remarks 5 and 7) and the SUPG test function option WTSE (see Remark 1). The stabilization parameters used are those given by Equations (14)–(21). The damping coefficient $\eta$ is set to



DOI: 10.1002/fld

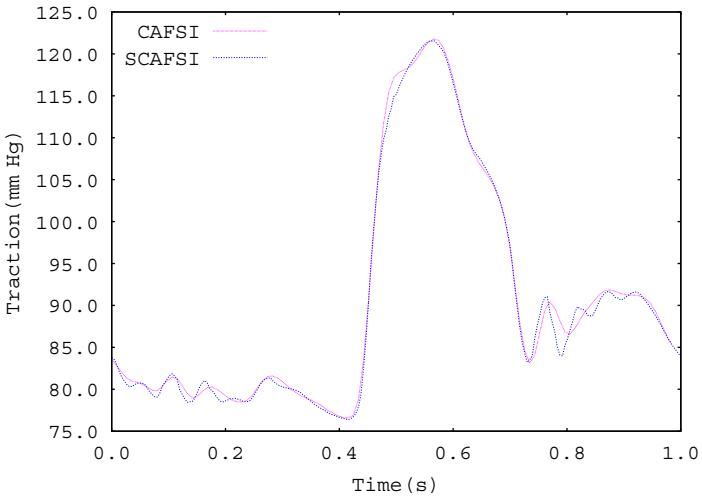


Figure 15. Abdominal aortic aneurysm. Comparison between the SCAFSI and CAFSI techniques. Normal component of the interface stress.

$5.65 \times 10^3\,\mathrm{s}^{-1}$. The time-step size is $4.4 \times 10^{-3}\,\mathrm{s}$. The number of nonlinear iterations per time step is 5, and the number of GMRES iterations per nonlinear iteration is 100. The $\mathrm{S} \rightarrow \mathrm{F} \rightarrow \mathrm{FSI}$ sequence is used in the computations.

Figure 11 shows the mass balance, and Figure 12 shows the flow field at approximately the same instants as those marked in Figure 5.

We computed this test case also with the SCAFSI technique (see Section 7). The computational parameters are almost the same as those we used for the fully coupled FSI (CAFSI) technique. The only differences are in the number of nonlinear iterations per time step, which is now 4, and the number of GMRES iterations per nonlinear iteration, which is now 25 for the structural mechanics part and 50 for the fluid mechanics part. The time-averaging weights in Step 3 of Section 7 are $(\omega_0, \omega_{\pm 1}, \omega_{\pm 2}, \omega_{\pm 3}, \omega_{\pm 4}) = \frac{1}{25}(5, 4, 3, 2, 1)$.

*Remark 11*

SCAFSI, unlike CAFSI, is not a fully coupled algorithm and therefore is underdamped. Because of that, it is more sensitive to any lack of smoothness in the inflow velocity profile, which was generated by digitizing the published data (see Section 8.1). To compensate for that, the inflow velocity profile for SCAFSI was modified very slightly to yield a smoother acceleration. In a way, this can partially be seen as restoring some of the smoothness lost during the digitization of the published data.

Figure 13 shows the mass balance obtained from the computation with the SCAFSI technique, which is quite good. The flow field looks essentially the same as what we displayed in Figure 12 for the CAFSI technique. Figures 14 and 15 show the comparison between the SCAFSI and CAFSI techniques based on the arterial volume and the normal component of the interface stress, respectively, and the results are quite close.



DOI: 10.1002/fld

## 9. CONCLUDING REMARKS

We presented an overview of how we model the arterial fluid mechanics problems with the stabilized space–time fluid–structure interaction (SSTFSI) technique developed by the T★AFSM. The SSTFSI technique includes the enhancements introduced recently by the T★AFSM to increase the scope, accuracy, robustness and efficiency of this class of techniques. The aspects of the FSI solution process enhanced include the DSD/SST formulation, which now has a number of new versions that render the earlier versions obsolete. The SSTFSI technique has been supplemented with a number of special techniques targeting specifically arterial fluid mechanics modeling. These include using an estimated zero-pressure arterial geometry, a recipe for pre-FSI computations that improve the convergence of the FSI computations, and the sequentially coupled arterial FSI (SCAFSI) technique. We need an estimated zero-pressure arterial geometry, because the patient-specific image-based geometries do not correspond to a zero blood pressure but time-averaged blood pressure values. The recipe for pre-FSI computations is based on the assumption that the arterial deformation during a cardiac cycle is driven mostly by the blood pressure. The SCAFSI technique, introduced as an approximate FSI approach specific to arterial fluid mechanics, is also based on that assumption. The arterial walls can be modeled with the membrane or continuum elements, both of which are geometrically nonlinear, and the continuum element is made of hyperelastic (Fung) material. We presented test computations for cerebral and abdominal aortic aneurysms. The arterial geometries used in the computations were close approximations to the patient-specific image-based data. With the test computations presented, we showed that the new SSTFSI techniques can successfully deal with different types of arterial fluid mechanics problems and structure models.

ACKNOWLEDGEMENTS

This work was supported in part by a Seed Grant from the Gulf Coast Center for Computational Cancer Research funded by John & Ann Doerr Fund for Computational Biomedicine. It was also supported in part by the Rice Computational Research Cluster funded by NSF under Grant CNS-0421109, and a partnership between Rice University, AMD and Cray. Portions of this work were supported by NIH/NHLBI Grant HL73868 (B.S. Conklin) and USDA 6250-51000-046 through the Children's Nutrition Research Center.

REFERENCES

1. Torii R, Oshima M, Kobayashi T, Takagi K, Tezduyar TE. Influence of wall elasticity on image-based blood flow simulation. *Japan Society of Mechanical Engineers Journal Series A* 2004; **70**:1224–1231 (in Japanese).
2. Torii R, Oshima M, Kobayashi T, Takagi K, Tezduyar TE. Computation of cardiovascular fluid–structure interactions with the DSD/SST method. *Proceedings of the 6th World Congress on Computational Mechanics* (*CD-ROM*), Beijing, China, 2004.
3. Gerbeau J-F, Vidrascu M, Frey P. Fluid–structure interaction in blood flow on geometries based on medical images. *Computers and Structures* 2005; **83**:155–165.
4. Torii R, Oshima M, Kobayashi T, Takagi K, Tezduyar TE. Computer modeling of cardiovascular fluid–structure interactions with the deforming-spatial-domain/stabilized space–time formulation. *Computer Methods in Applied Mechanics and Engineering* 2006; **195**:1885–1895.
5. Torii R, Oshima M, Kobayashi T, Takagi K, Tezduyar TE. Fluid–structure interaction modeling of aneurysmal conditions with high and normal blood pressures. *Computational Mechanics* 2006; **38**:482–490.
6. Bazilevs Y, Calo VM, Zhang Y, Hughes TJR. Isogeometric fluid–structure interaction analysis with applications to arterial blood flow. *Computational Mechanics* 2006; **38**:310–322.



DOI: 10.1002/fld

7. Torii R, Oshima M, Kobayashi T, Takagi K, Tezduyar TE. Influence of wall elasticity in patient-specific hemodynamic simulations. *Computers and Fluids* 2007; **36**:160–168.
8. Tezduyar TE, Sathe S, Cragin T, Nanna B, Conklin BS, Pausewang J, Schwaab M. Modeling of fluid–structure interactions with the space–time finite elements: arterial fluid mechanics. *International Journal for Numerical Methods in Fluids* 2007; **54**:901–922.
9. Bazilevs Y, Calo VM, Tezduyar TE, Hughes TJR. YZ$\beta$ discontinuity-capturing for advection-dominated processes with application to arterial drug delivery. *International Journal for Numerical Methods in Fluids* 2007; **54**: 593–608.
10. Torii R, Oshima M, Kobayashi T, Takagi K, Tezduyar TE. Numerical investigation of the effect of hypertensive blood pressure on cerebral aneurysm—dependence of the effect on the aneurysm shape. *International Journal for Numerical Methods in Fluids* 2007; **54**:995–1009.
11. Tezduyar TE. Stabilized finite element formulations for incompressible flow computations. *Advances in Applied Mechanics* 1992; **28**:1–44.
12. Tezduyar TE, Behr M, Liou J. A new strategy for finite element computations involving moving boundaries and interfaces—the deforming-spatial-domain/space–time procedure: I. The concept and the preliminary numerical tests. *Computer Methods in Applied Mechanics and Engineering* 1992; **94**:339–351.
13. Tezduyar TE, Behr M, Mittal S, Liou J. A new strategy for finite element computations involving moving boundaries and interfaces—the deforming-spatial-domain/space–time procedure: II. Computation of free-surface flows, two-liquid flows, and flows with drifting cylinders. *Computer Methods in Applied Mechanics and Engineering* 1992; **94**:353–371.
14. Mittal S, Tezduyar TE. Parallel finite element simulation of 3D incompressible flows—fluid–structure interactions. *International Journal for Numerical Methods in Fluids* 1995; **21**:933–953.
15. Kalro V, Tezduyar TE. A parallel 3D computational method for fluid–structure interactions in parachute systems. *Computer Methods in Applied Mechanics and Engineering* 2000; **190**:321–332.
16. Stein K, Benney R, Kalro V, Tezduyar TE, Leonard J, Accorsi M. Parachute fluid–structure interactions: 3-D computation. *Computer Methods in Applied Mechanics and Engineering* 2000; **190**:373–386.
17. Tezduyar T, Osawa Y. Fluid–structure interactions of a parachute crossing the far wake of an aircraft. *Computer Methods in Applied Mechanics and Engineering* 2001; **191**:717–726.
18. Ohayon R. Reduced symmetric models for modal analysis of internal structural-acoustic and hydroelastic-sloshing systems. *Computer Methods in Applied Mechanics and Engineering* 2001; **190**:3009–3019.
19. Tezduyar TE. Computation of moving boundaries and interfaces and stabilization parameters. *International Journal for Numerical Methods in Fluids* 2003; **43**:555–575.
20. Michler C, van Brummelen EH, Hulshoff SJ, de Borst R. The relevance of conservation for stability and accuracy of numerical methods for fluid–structure interaction. *Computer Methods in Applied Mechanics and Engineering* 2003; **192**:4195–4215.
21. Gerbeau J-F, Vidrascu M. A quasi-Newton algorithm based on a reduced model for fluid–structure interaction problems in blood flows. *Mathematical Modelling and Numerical Analysis* 2003; **37**:663–680.
22. Tezduyar TE, Sathe S, Keedy R, Stein K. Space–time techniques for finite element computation of flows with moving boundaries and interfaces. In *Proceedings of the III International Congress on Numerical Methods in Engineering and Applied Science*, CD-ROM, Monterrey, Mexico, Gallegos S, Herrera I, Botello S, Zarate F, Ayala G (eds). 2004.
23. Hubner B, Walhorn E, Dinkler D. A monolithic approach to fluid–structure interaction using space–time finite elements. *Computer Methods in Applied Mechanics and Engineering* 2004; **193**:2087–2104.
24. Michler C, van Brummelen EH, Hulshoff SJ, de Borst R. A monolithic approach to fluid–structure interaction. *Computers and Fluids* 2004; **33**:839–848.
25. Tezduyar TE, Sathe S, Senga M, Aureli L, Stein K, Griffin B. Finite element modeling of fluid–structure interactions with space–time and advanced mesh update techniques. *Proceedings of the 10th International Conference on Numerical Methods in Continuum Mechanics* (*CD-ROM*), Zilina, Slovakia, 2005.
26. van Brummelen EH, de Borst R. On the nonnormality of subiteration for a fluid–structure interaction problem. *SIAM Journal on Scientific Computing* 2005; **27**:599–621.
27. Michler C, van Brummelen EH, de Borst R. An interface Newton–Krylov solver for fluid–structure interaction. *International Journal for Numerical Methods in Fluids* 2005; **47**:1189–1195.
28. Fernandez MA, Moubachir M. A Newton method using exact Jacobians for solving fluid–structure coupling. *Computers and Structures* 2005; **83**:127–142.
29. Tezduyar TE, Sathe S, Keedy R, Stein K. Space–time finite element techniques for computation of fluid–structure interactions. *Computer Methods in Applied Mechanics and Engineering* 2006; **195**:2002–2027.




DOI: 10.1002/fld

30. Tezduyar TE, Sathe S, Stein K. Solution techniques for the fully-discretized equations in computation of fluid–structure interactions with the space–time formulations. *Computer Methods in Applied Mechanics and Engineering* 2006; **195**:5743–5753.
31. Masud A, Khurram RA. A multiscale finite element method for the incompressible Navier–Stokes equations. *Computer Methods in Applied Mechanics and Engineering* 2006; **195**:1750–1777.
32. Khurram RA, Masud A. A multiscale/stabilized formulation of the incompressible Navier–Stokes equations for moving boundary flows and fluid–structure interaction. *Computational Mechanics* 2006; **38**:403–416.
33. Masud A. Effects of mesh motion on the stability and convergence of ALE based formulations for moving boundary flows. *Computational Mechanics* 2006; **38**:430–439.
34. Kuttler U, Forster C, Wall WA. A solution for the incompressibility dilemma in partitioned fluid–structure interaction with pure Dirichlet fluid domains. *Computational Mechanics* 2006; **38**:417–429.
35. Dettmer W, Peric D. A computational framework for fluid–rigid body interaction: finite element formulation and applications. *Computer Methods in Applied Mechanics and Engineering* 2006; **195**:1633–1666.
36. Tezduyar TE, Sathe S, Stein K, Aureli L. Modeling of fluid–structure interactions with the space–time techniques. In *Fluid–Structure Interaction*, Bungartz H-J, Schafer M (eds). Lecture Notes in Computational Science and Engineering, vol. 53. Springer: Berlin, 2006; 50–81.
37. Lohner R, Cebral JR, Yang C, Baum JD, Mestreau EL, Soto O. Extending the range of applicability of the loose coupling approach for FSI simulations. In *Fluid–Structure Interaction*, Bungartz HJ, Schafer M (eds). Lecture Notes in Computational Science and Engineering, vol. 53. Springer: Berlin, 2006; 82–100.
38. Wall WA, Gerstenberger A, Gamnitzer P, Forster C, Ramm E. Large deformation fluid–structure interaction–advances in ALE methods and new fixed grid approaches. In *Fluid–Structure Interaction*, Bungartz H-J, Schafer M (eds). Lecture Notes in Computational Science and Engineering, vol. 53. Springer: Berlin, 2006; 195–232.
39. Bletzinger K-U, Wuchner R, Kupzok A. Algorithmic treatment of shells and free form-membranes in FSI. In *Fluid–Structure Interaction*, Bungartz H-J, Schafer M (eds). Lecture Notes in Computational Science and Engineering, vol. 53. Springer: Berlin, 2006; 336–355.
40. Dettmer W, Peric D. A computational framework for fluid–structure interaction: finite element formulation and applications. *Computer Methods in Applied Mechanics and Engineering* 2006; **195**:5754–5779.
41. Masud A, Bhanabhagvanwala M, Khurram RA. An adaptive mesh rezoning scheme for moving boundary flows and fluid–structure interaction. *Computers and Fluids* 2007; **36**:77–91.
42. Sawada T, Hisada T. Fluid–structure interaction analysis of the two dimensional flag-in-wind problem by an interface tracking ALE finite element method. *Computers and Fluids* 2006; **36**:136–146.
43. Wall WA, Genkinger S, Ramm E. A strong coupling partitioned approach for fluid–structure interaction with free surfaces. *Computers and Fluids* 2007; **36**:169–183.
44. Hughes TJR, Liu WK, Zimmermann TK. Lagrangian–Eulerian finite element formulation for incompressible viscous flows. *Computer Methods in Applied Mechanics and Engineering* 1981; **29**:329–349.
45. Hughes TJR, Brooks AN. A multi-dimensional upwind scheme with no crosswind diffusion. In *Finite Element Methods for Convection Dominated Flows*, Hughes TJR (ed.). AMD-vol. 34. ASME: New York, 1979; 19–35.
46. Brooks AN, Hughes TJR. Streamline upwind/Petrov–Galerkin formulations for convection dominated flows with particular emphasis on the incompressible Navier–Stokes equations. *Computer Methods in Applied Mechanics and Engineering* 1982; **32**:199–259.
47. Tezduyar TE, Mittal S, Ray SE, Shih R. Incompressible flow computations with stabilized bilinear and linear equal-order-interpolation velocity–pressure elements. *Computer Methods in Applied Mechanics and Engineering* 1992; **95**:221–242.
48. Hughes TJR, Franca LP, Balestra M. A new finite element formulation for computational fluid dynamics: V. Circumventing the Babuška–Brezzi condition: a stable Petrov–Galerkin formulation of the Stokes problem accommodating equal-order interpolations. *Computer Methods in Applied Mechanics and Engineering* 1986; **59**:85–99.
49. Hulbert TJR, Hughes GM. Space–time finite element methods for elastodynamics: formulations and error estimates. *Computer Methods in Applied Mechanics and Engineering* 1988; **66**:339–363.
50. Tezduyar TE, Behr M, Mittal S, Johnson AA. Computation of unsteady incompressible flows with the finite element methods—space–time formulations, iterative strategies and massively parallel implementations. *New Methods in Transient Analysis*, PVP-vol. 246/AMD-vol. 143. ASME: New York, 1992; 7–24.
51. Johnson AA, Tezduyar TE. Mesh update strategies in parallel finite element computations of flow problems with moving boundaries and interfaces. *Computer Methods in Applied Mechanics and Engineering* 1994; **119**:73–94.
52. Tezduyar TE. Finite element methods for flow problems with moving boundaries and interfaces. *Archives of Computational Methods in Engineering* 2001; **8**:83–130.



DOI: 10.1002/fld

53. Tezduyar TE, Sathe S. Modeling of fluid–structure interactions with the space–time finite elements: solution techniques. *International Journal for Numerical Methods in Fluids* 2007; **54**:855–900.
54. Hughes TJR. Personal communication, February 2007.
55. Tezduyar TE, Cragin T, Sathe S, Nanna B. Arterial fluid mechanics with the SSTFSI technique and continuum element made of hyperelastic (Mooney–Rivlin) material. In *Coupled Problems 2007*, Onate E, Papadrakakis M, Schrefler B (eds). CIMNE: Barcelona, Spain, 2007.
56. Prendergast PJ, Lally C, Daly S, Reid AJ, Lee TC, Quinn D, Dolan F. Analysis of prolapse in cardiovascular stents: a constitutive equation for vascular tissue and finite-element modelling. *Journal of Biomechanical Engineering* 2003; **125**:692–699.
57. Tezduyar TE, Cragin T, Sathe S, Nanna B. FSI computations in arterial fluid mechanics with estimated zero-pressure arterial geometry. In *Marine 2007*, Onate E, Garcia J, Bergan P, Kvamsdal T (eds). CIMNE: Barcelona, Spain, 2007.
58. Tezduyar TE, Schwaab M, Sathe S. Arterial fluid mechanics with the sequentially-coupled arterial FSI technique. In *Coupled Problems 2007*, Onate E, Papadrakakis M, Schrefler B (eds). CIMNE: Barcelona, Spain, 2007.
59. Wells Jr RE, Merrill EW. Shear rate dependence of the viscosity of whole blood and plasma. *Science* 1961; **133**:763–764.
60. Betsch P, Gruttmann F, Stein E. A 4-node finite shell element for the implementation of general hyperelastic 3d-elasticity at finite strains. *Computer Methods in Applied Mechanics and Engineering* 1996; **130**:57–79.
61. Stuparu M. Human heart valves. Hyperelastic material modeling. *Proceedings of the Xth Conference on Mechanical Vibrations*, Timisoara, Romania, 2002.
62. Tezduyar TE, Osawa Y. Finite element stabilization parameters computed from element matrices and vectors. *Computer Methods in Applied Mechanics and Engineering* 2000; **190**:411–430.
63. Tezduyar TE. Finite element methods for fluid dynamics with moving boundaries and interfaces. In *Encyclopedia of Computational Mechanics*, *Volume 3*: *Fluids*, Chapter 17, Stein E, De Borst R, Hughes TJR (eds). Wiley: New York, 2004.
64. Tezduyar TE, Finite elements in fluids: stabilized formulations and moving boundaries and interfaces. *Computers and Fluids* 2007; **36**:191–206.
65. Lo A. Nonlinear dynamic analysis of cable and membrane structure. *Ph.D. Thesis*, Department of Civil Engineering, Oregon State University, 1982.
66. Benney RJ, Stein KR, Leonard JW, Accorsi ML. Current 3-D structural dynamic finite element modeling capabilities. *Proceedings of AIAA 14th Aerodynamic Decelerator Systems Technology Conference*, AIAA Paper 97-1506, San Francisco, CA, 1997.
67. Hilber HM, Hughes TJR, Taylor RL. Improved numerical dissipation for time integration algorithms in structural dynamics. *Earthquake Engineering and Structural Dynamics* 1977; **5**:283–292.
68. Tezduyar T, Aliabadi S, Behr M, Johnson A, Mittal S. Parallel finite-element computation of 3D flows. *Computer* 1993; **26**:27–36.
69. Johnson AA, Tezduyar TE. Simulation of multiple spheres falling in a liquid-filled tube. *Computer Methods in Applied Mechanics and Engineering* 1996; **134**:351–373.
70. Tezduyar T. Finite element interface-tracking and interface-capturing techniques for flows with moving boundaries and interfaces. *Proceedings of the ASME Symposium on Fluid-Physics and Heat Transfer for Macro- and Micro-scale Gas–liquid and Phase-change Flows* (*CD-ROM*), ASME Paper IMECE2001/HTD-24206. ASME: New York, NY, 2001.
71. Tezduyar TE. Stabilized finite element formulations and interface-tracking and interface-capturing techniques for incompressible flows. In *Numerical Simulations of Incompressible Flows*, Hafez MM (ed.). World Scientific: New Jersey, 2003; 221–239.
72. Stein K, Tezduyar T, Benney R. Mesh moving techniques for fluid–structure interactions with large displacements. *Journal of Applied Mechanics* 2003; **70**:58–63.
73. Stein K, Tezduyar T. Advanced mesh update techniques for problems involving large displacements. *Proceedings of the Fifth World Congress on Computational Mechanics*, On-line publication: http://wccm.tuwien.ac.at/, Paper-ID: 81489, Vienna, Austria, 2002.
74. Stein K, Tezduyar TE, Benney R. Automatic mesh update with the solid-extension mesh moving technique. *Computer Methods in Applied Mechanics and Engineering* 2004; **193**:2019–2032.
75. Lynch DR. Wakes in liquid–liquid systems. *Journal of Computational Physics* 1982; **47**:387–411.
76. Masud A, Hughes TJR. A space–time Galerkin/least-squares finite element formulation of the Navier–Stokes equations for moving domain problems. *Computer Methods in Applied Mechanics and Engineering* 1997; **146**:91–126.



DOI: 10.1002/fld

77. Fujisawa T, Inaba M, Yagawa G. Parallel computing of high-speed compressible flows using a node-based finite element method. *International Journal for Numerical Methods in Fluids* 2003; **58**:481–511.
78. Tezduyar TE. Stabilized finite element methods for computation of flows with moving boundaries and interfaces. *Lecture Notes on Finite Element Simulation of Flow Problems* (*Basic—Advanced Course*). Japan Society of Computational Engineering and Sciences, Tokyo, Japan, 2003.
79. Tezduyar TE. Stabilized finite element methods for flows with moving boundaries and interfaces. *HERMIS*: *The International Journal of Computer Mathematics and its Applications* 2003; **4**:63–88.
80. Tezduyar TE. Moving boundaries and interfaces. In *Finite Element Methods*: *1970's and Beyond*, Franca LP, Tezduyar TE, Masud A (eds). CIMNE: Barcelona, Spain, 2004; 205–220.
81. Tezduyar TE. Finite elements in fluids: special methods and enhanced solution techniques. *Computers and Fluids* 2007; **36**:207–223.
82. Saad Y, Schultz M. GMRES: a generalized minimal residual algorithm for solving nonsymmetric linear systems. *SIAM Journal on Scientific and Statistical Computing* 1986; **7**:856–869.
83. Johan Z, Hughes TJR, Shakib F. A globally convergent matrix-free algorithm for implicit time-marching schemes arising in finite element analysis in fluids. *Computer Methods in Applied Mechanics and Engineering* 1991; **87**:281–304.
84. Johan Z, Mathur KK, Johnsson SL, Hughes TJR. A case study in parallel computation: viscous flow around an Onera M6 wing. *International Journal for Numerical Methods in Fluids* 1995; **21**:877–884.
85. Sameh A, Manguoglu M, Sathe S, Tezduyar TE. A nested iterative scheme for nonsymmetric linear systems. In *Coupled Problems 2007*, Onate E, Papadrakakis M, Schrefler B (eds). CIMNE: Barcelona, Spain, 2007.
86. Sameh A, Manguoglu M, Sathe S, Pausewang J, Tezduyar TE. Iterative techniques with banded preconditioners for fluid mechanics computations over long domains. In *Marine 2007*, Onate E, Garcia J, Bergan P, Kvamsdal T (eds). CIMNE: Barcelona, Spain, 2007.
87. Tezduyar TE, Liou J, Ganjoo DK. Incompressible flow computations based on the vorticity-stream function and velocity–pressure formulations. *Computers and Structures* 1990; **35**:445–472.
88. Tezduyar TE, Mittal S, Shih R. Time-accurate incompressible flow computations with quadrilateral velocity–pressure elements. *Computer Methods in Applied Mechanics and Engineering* 1991; **87**:363–384.
89. Sameh A, Sarin V. Hybrid parallel linear solvers. *International Journal of Computational Fluid Dynamics* 1991; **12**:213–223.
90. Sameh A, Sarin V. Parallel algorithms for indefinite linear systems. *Parallel Computing* 2002; **28**:285–299.
91. Womersley JR. Method for the calculation of velocity, rate of flow and viscos drag in arteries when the pressure gradient is known. *Journal of Physiology* 1955; **127**:553–563.
92. Otto F. Die grundform des arteriellen pulses. *Zeitung fur Biologie* 1899; **37**:483–586.
93. Huang H, Virmani R, Younis H, Burke AP, Kamm RD, Lee RT. The impact of calcification on the biomechanical stability of atherosclerotic plaques. *Circulation* 2001; **103**:1051–1056.
94. Elguedj T, Bazilevs Y, Calo VM, Hughes TJR. B-bar and F-bar projection methods for nearly incompressible linear and nonlinear elasticity and plasticity using higher-order nurbs elements. *Computer Methods in Applied Mechanics and Engineering* 2007, submitted.
95. Available from: http://www.vascularweb.org/_CONTRIBUTION_PAGES/Patient_Information/3_Most_Common_AVA/AorticAneurysms_AVA.html.
96. Available from: http://www.slrsurgery.org/divisions/vascular.html.
97. Available from: http://www.camsf.com/vasc_aortic.html.
98. Li AE, Kamel I, Rando F, Anderson M, Lima JAC, Kumbasar B, Bluemke DA. Using MRI to assess aortic wall thickness in the multiethnic study of atherosclerosis: distribution by race, sex, and age. *American Journal of Roentgenology* 2004; **182**:593–597.
99. Rowland T, Potts J, Potts T, Son-Hing J, Harbison G, Sandor G. Cardiovascular responses to exercise in children and adolescents with myocardial dysfunction. *American Heart Journal* 1999; **137**:126–133.



DOI: 10.1002/fld